Fall 2022

MANTLE FLOW AND TRANSITION ZONE DISCONTINUITIES BENEATH THE CARRIBEAN PLATE: CONSTRAINTS FROM SHEAR WAVE SPLITTING AND RECEIVER FUNCTION ANALYSES

Tu Xue
Missouri University of Science and Technology

Department: Geosciences and Geological and Petroleum Engineering

Recommended Citation

Xue, Tu, "MANTLE FLOW AND TRANSITION ZONE DISCONTINUITIES BENEATH THE CARRIBEAN PLATE: CONSTRAINTS FROM SHEAR WAVE SPLITTING AND RECEIVER FUNCTION ANALYSES" (2022). *Doctoral Dissertations*. 3242.
https://scholarsmine.mst.edu/doctoral_dissertations/3242

MANTLE FLOW AND TRANSITION ZONE DISCONTINUITIES BENEATH THE CARRIBEAN PLATE: CONSTRAINTS FROM SHEAR WAVE SPLITTING AND RECEIVER FUNCTION ANALYSES

by

TU XUE

A DISSERTATION

Presented to the Graduate Faculty of the

MISSOURI UNIVERSITY OF SCIENCE AND TECHNOLOGY

In Partial Fulfillment of the Requirements for the Degree

DOCTOR OF PHILOSOPHY

in

GEOLOGY AND GEOPHYSICS

2022

Approved by:

Stephen S. Gao, Advisor
Kelly H. Liu, Co-Advisor
J. David Rogers
Kevin L. Mickus
Jonathan Obrist Farner
Yutao Shi

PUBLICATION DISSERTATION OPTION

This dissertation consists of the following two articles, formatted in the style used by the Missouri University of Science and Technology:

Paper I, found on pages 3–29, is intended for submission to *Natural Geoscience*.

Paper II, found on pages 30–49, is intended for submission to *Geology*.

ABSTRACT

Azimuthal anisotropy quantified by teleseismic *SKS, SKKS, PKS* (“*XKS*”) and local *S* wave splitting parameters is used to investigate lithospheric deformation and asthenospheric flow beneath the boundary zone of the North American and Caribbean plates and adjacent areas. A total of 4915 *XKS* and 1202 pairs of local *S* wave splitting parameters were obtained at 24 broad band seismic stations. The *XKS* observations can be divided into two groups based on the spatial distribution of the resulting fast polarization orientations. Those observed on the Caribbean Plate are mostly WNW-ESE which are roughly trench-parallel. In contrast, the fast orientations observed on the North American Plate are dominantly NNE-SSW which are approximately trench-orthogonal and are consistent with those previously observed in southern Mexico to the north of the area of the current study. At most of the stations at which *XKS* and local *S* wave splitting parameters are available, the fast orientations from the two types of shear waves are comparable, but the *XKS* splitting times are about twice of the local *S* wave splitting times, suggesting that the observed azimuthal anisotropy has contributions from both above and below the subducting oceanic slab. In the Lesser Antilles subduction zone, a thinner than normal transition zone thickness is revealed and is attributable to mantle upwelling along the edges of the slab and slab gaps beneath the area. The transition zone thinning is mostly caused by an uplifted 660 km discontinuity, suggesting that the thermal upwelling may be originated from the lower mantle of the Earth. The uplifted 410 km and depressed 660 km discontinuities in area south of the southern boundary of the Caribbean plate may indicate the existence of cold slab segments.

ACKNOWLEDGMENTS

I would like to thank my advisor Dr. Stephen S. Gao for his invaluable advice and patience during my PhD study. Dr. Gao continuously provided encouragement and was always willing and enthusiastic to assist in any way he could throughout my PhD study. His immense knowledge and plentiful experience have encouraged me in all time of my academic research and daily life.

I would also like to express my thanks to my co-advisor Dr. Kelly H. Liu for her dedicated support and guidance. Her overall insights in my research field have made this an inspiring experience for me. I am also grateful to my committee members: Dr. J. David Rogers. Dr. Kevin L. Mickus, Dr. Jonathan Obrist Farner, Dr. Yutao Shi for their thoughtful comments and recommendations on my research study. In addition, I would like to thank my colleagues and friends in the Geophysics Group who helped me a lot during the past five years.

Finally, I am indebted to my parents for their love and help. Without their tremendous understanding and encouragement in the past few years, it would be impossible for me to complete my study.

TABLE OF CONTENTS

Page

SECTION

PAPER

SECTION

LIST OF ILLUSTRATIONS

PAPER I Page

PAPER II

LIST OF TABLES

PAPER I

NOMENCLATURE

Symbol	Description
PAPER II	
MC	Cut-off Magnitude
Δ	Epicentral distance in degree
D	Focal Depth

1. INTRODUCTION

The Caribbean (CA) Plate is surrounded by the North American (NA) Plate to the north, the South American (SA) Plate to the east and south, the Nazca (NZ) Plate to the southwest, and the Cocos (CO) Plate to the west. The subduction of the Farallon lithosphere beneath the American Plate, which was separated into the NA and SA Plates during the Jurassic (Ladd, 1976), started in the early Cretaceous (Pindell & Barrett, 1990). The interaction among the plates resulted in a complex evolutionary history of the CA Plate and surrounding plate boundary zones, whose origin has been described by two major models. The ‘*Pacific*’ model proposes that the CA Plate originated within the Farallon Plate, and as a result of the subduction of the Farallon Plate, the CA Plate later moved to its present position between the two American Plates (Pindell & Barrett, 1990). In contrast, the ‘*Intra-Americans*’ model suggests that the CA Plate originated between the NA and SA Plates as the results of fragmentation of the American Plate (Meschede & Frisch, 1998). From the Late Cretaceous until the Eocene, the Atlantic lithosphere subducted westward beneath the eastern boundary of the CA Plate. This subduction created the *Great Arc of the Caribbean*, which is a remnant arc and is currently the Great Antilles (Laurencin et al., 2018). The subduction also created an active arc, the Lesser Antilles arc (Laurencin et al., 2018). The west-dipping subduction of the Atlantic lithosphere beneath the Lesser Antilles continues from the Eocene until the present (van Benethem et al., 2013a).

The dissertation is mainly composed of two parts. The first part investigated seismic anisotropy in Central America and adjacent areas. In the southern Mexico portion of the NA Plate, the observed fast orientations are mostly NE-SW, i.e., orthogonal to the orientation of the MAT. Two mechanisms have been proposed to explain the observed trench-perpendicular anisotropy. For areas where the Cocos slab dips steeply, the observed anisotropy is attributed to a 2-D corner flow system driven by the down-dip motion of the slab (Bernal-López et al., 2016; van Benthem et al., 2013b). In contrast, in the area underlain by the flat-subducting slab, the observed anisotropy is thought to be associated with a sub-slab entrained flow in the direction of the plate motion (Bernal-López et al., 2016; León Soto et al., 2013; van Benthem et al., 2013b; Castellanos et al., 2017).

The second part demonstrated that the topography of 410 km and 660 km discontinuities (hereafter referred to as *d*410 and *d*660). Using the waveform data from the BOLIVAR project (Levander et al., 2006), Huang et al. (2010) image the *d*410 and *d*660 beneath the CA-SA Plate boundary, which is in the southeast corner of our study area. The seismic images show that the westward subduction of the oceanic SA Plate causes an up to ~ 25 km uplift of the d410 and ~ 20 km depression to the *d*660. In addition, an uplifted *d*410 at the western end of the CA-SA Plate boundary in Venezuela is attributed to the subduction of the NZ Plate (Huang et al., 2010). In this study, we use RFs to image the 410 and 660 km discontinuities and map the spatial variation of the thickness of the MTZ, for purpose of detecting the existence and spatial distribution of subducted slabs and mantle upwelling in eastern Caribbean.

PAPER

I. ONGOING FRAGMENTATION OF THE SUBDUCTING COCOS SLAB

ABSTRACT

Fundamental to plate tectonics is the subduction of cold and mechanically strong oceanic plates. While the subducted plates are conventionally regarded to be impermeable to mantle flow that separate the mantle wedge and the subslab region, isolated openings (termed slab gaps hereinafter) have been proposed. Here, by combining new shear wave splitting measurements with recent seismic tomography and geochemical observations, we show that the top ~200 km of the Cocos slab in northern Central America is intensively fractured, probably by orthogonally oriented compressional stresses associated with seafloor spreading from the East Pacific Rise and the Galapagos Spreading Center at the western and southern edges of the slab, respectively. The pervious slab is strong enough to produce typical arc volcanoes and Benioff Zone earthquakes but allows mantle flow to traverse from the subslab region to the mantle wedge. Upwelling of hot subslab mantle flow through the slab provides a viable explanation for the behind the arc volcanoes that are geochemically distinct from typical arc volcanoes, and for the puzzling high heat flow, high elevation, and low gravity anomalies observed in the area.

1. INTRODUCTION

The Cocos Plate is bounded by the East Pacific Rise on the west and the Galapagos spreading center to the south (Figure 1). It was formed when the Farallon Plate broke into two pieces at about 23 million years ago (Pardo and Suárez, 1995; Dougherty et al., 2012; Borgeaud et al., 2018). Compared with most other convergent plate boundary zones, northern Central America, where the Cocos Plate is subducting beneath the North American and Caribbean Plates, has several puzzling observations including the anomalously high topography (Rogers et al., 2002), high heat flow (Peacocks et al., 2005), low Bouguer gravity anomalies (Supplementary Figure. S1), and the presence of intraplate Cenozoic volcanoes in eastern Guatemala and western El Salvador (Figure 1). A compilation of measurements from existing geochemical studies indicates that the primitive-mantle-normalized trace element patterns from samples from the volcanic front (VF) and behind the volcanic front (BVF) are notably different (Figure 2a). The VF lavas display features commonly associated with hydrous magmas derived from a subducting slab, most notably a distinct negative trough in Nb and Ta. Conversely, the absence of negative Nb and Ta anomalies in BVF lavas, combined with high contents of light rare earth elements that display a steeper decline from La to Sm when compared to VF, suggest that the BVF lavas formed from low degrees of partial melting of a protolith without significant water contents. Another unusual feature of this area is the lack of deep-focus earthquakes and a reduction in earthquake productivity in the depth range of ~100-200 km relative to the world's subduction zones (Figure 2b).

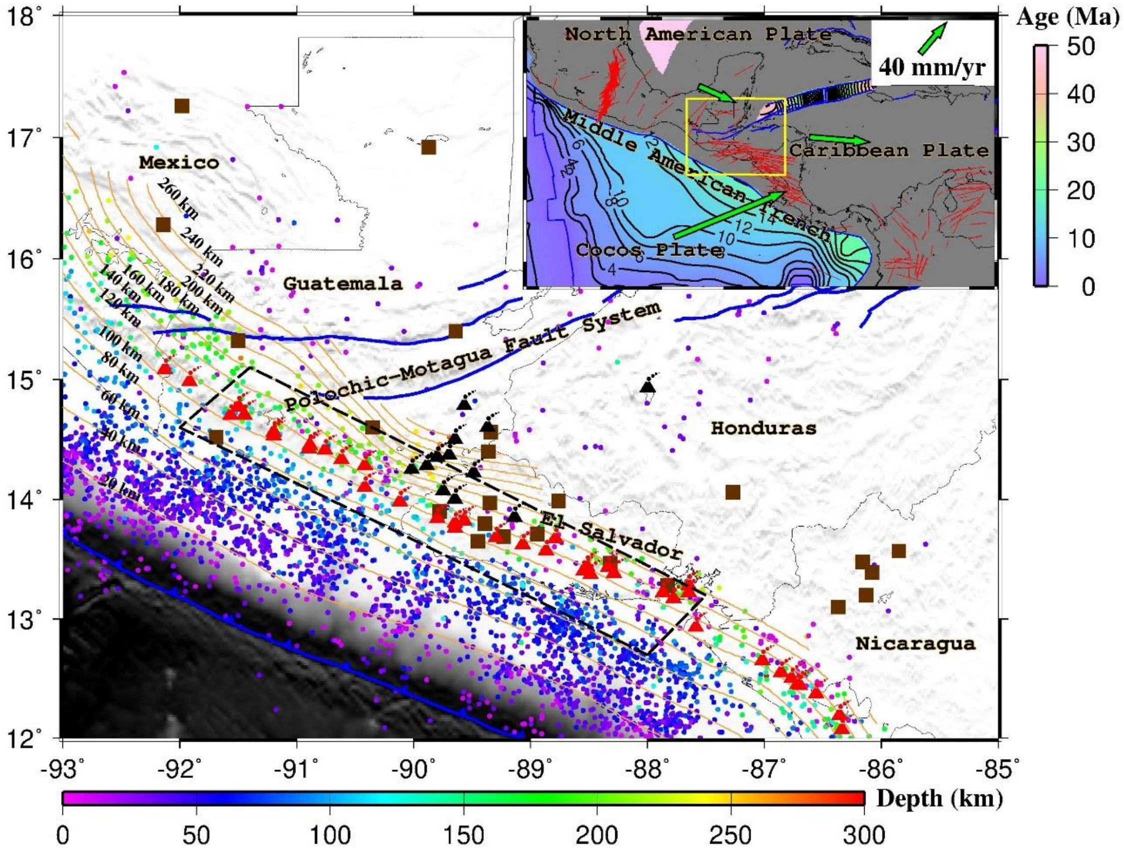

Figure 1. Tectonic setting of northern Central America. The brown squares show the seismic stations used in the study. The red triangles represent arc-front volcanoes, the black triangles represent back-arc volcanoes, and the colored dots represent the epicenters and focal depths of Magnitude 4.5 and greater earthquakes occurred between 1980 and 2022. The yellow contour lines show the depths of the Cocos slab. The area outlined by the dashed lines indicates the approximate extent of the proposed pervious slab. The enclosed region in the inset map shows the study area, where the contour lines show the ocean floor ages. The red bars represent results from our shear wave splitting study results and previous studies (van Benthem et al., 2013b; Abt et al., 2010; Russo & Silver, 1994; Masy et al., 2011; Bernal-Lopez et al., 2015; Porrit et al., 2014; Idarraga-Garcia et al., 2016; Castellanos et al., 2017; Pinero-Feliciangeli & Kendall, 2008). The orientations of the bars show the fast polarization orientation, and the length of the bars is proportional to the splitting time.

Mostly due to the poor coverage by seismic stations in the area and the resulting low resolution of seismic tomographic images, conflicting conclusions regarding the continuity and geometry of the Cocos slab have been reached by different tomography studies. Based on a global-scale P-wave velocity model, Rogers et al. (2002) proposed the existence of a slab gap in the depth range of 200-500 km and horizontally spanning a total length of ~900km from southern Mexico to Honduras and attributed the high elevation in the back-arc area to upwelling mantle flow from this slab gap. This model, however, is inconsistent with more recent tomographic images. For instance, a regional-scale full-waveform inversion study (Zhu et al., 2020) revealed a continuous Cocos slab extending from the surface to the depth of at least 1000 km. However, the same study also found that in the top 200 km, the velocity anomaly of the slab is significantly smaller than the deeper sections of the slab (Supplementary Figure S2), consistent with the reduced seismicity around this depth (Figure. 2b). In addition, the dominant fast orientation of seismic anisotropy at the depths greater than 80 km is different between the oceanic and continental sides (i.e., trench perpendicular on the Cocos and trench parallel on the Caribbean plates) and becomes, which represents the sublithospheric mantle, E-W for both the oceanic and continental sides (Supplementary Figure S3). Such a continuity of fast orientations suggests similarly oriented flow paths from the subslab region to the mantle wedge across the Cocos slab.

2. CONSTRAINTS ON THE MANTLE FLOW FIELDS FROM SHEAR WAVE SPLITTING ANALYSES

In addition to seismic tomography, numerous studies have demonstrated that the mantle flow system in the vicinity of a subducting slab can be delineated by analyzing the splitting of shear waves (Hess, 1964; Silver and Chan, 1991; Long and Silver, 2009; Zhou et al., 2018; Kong et al., 2022). Relative to seismic tomography, shear wave splitting has a higher lateral and lower vertical resolution, although the latter can be partially improved by using earthquakes at teleseismic distance and those occurred locally along the subducting slab (see the Methods section). In Nicaragua and Costa Rica which are located to the southeast of the study area, the fast orientations for both teleseismic and local S waves are largely trench parallel and are interpreted as being caused by along-trench flow in the mantle wedge and beneath the slab (Abt et al., 2009; 2010). In contract, the fast orientations in southern Mexico are dominantly trench perpendicular and are interpreted as reflecting subduction-induced corner flow in the mantle wedge (Figure 1; Bernal-López et al., 2016). Both trench parallel and trench perpendicular fast orientations are pervasively observed in other subduction zones in the world (Long and Silver, 2009).

Our observations from teleseismics for the Caribbean Plate are neither trench parallel nor trench perpendicular (Figure 3). More intriguingly, observations at stations located on the southwestern side of the volcanic arc show a clear piercing point dependence (Jia et al., 2021). In particular, the fast orientations tend to be more trench perpendicular for ray paths arriving at the stations from the SW than those from other back-azimuths. This clockwise rotation of the inferred mantle flow directions is consistent with results from a full-waveform inversion (Zhu et al., 2020) (Supplementary Figure S3). In contrast to the teleseismic results, the fast orientations measured from earthquakes occurred along the subducting slab (and thus the ray paths sample the mantle wedge and the overriding plate) are mostly trench parallel. Another notable feature is a sudden change in anisotropy orientations across the North American-Caribbean Plate boundaries, where results in the northern part are more trench-normal that resembles typical wedge flow. This implies an abnormal flow pattern below the Caribbean Plate.

3. NUMERIC SIMULATION OF CENOZOIC COCOS SUBDUCTION

To quantitatively evaluate the subduction dynamics of the Cocos plate, we perform numerical models with data-assimilation (Liu & Stegman, 2011) that satisfy the observed Cenozoic plate motion history and sea floor ages (See Method for more details). Tests show that simulations starting no later than 40 Ma produce similar present-day slab structure and mantle flow. Here we present the result from a case that covers subduction since 45 Ma. We find that below the study area, the central portion of the Cocos slab experienced gradual shallowing since ~30 Ma and eventually developed a central slab tear along the slab hinge at the present (Figure. 4a, 4b). The present slab geometry, including both a highly extended thin slab above 200 km depth and the larger slab pile further down, matches the recent seismic tomography well (Figure. 4c).

Physically, the gradual dip angle reduction leading to a final slab tear below our study region reflects the sub-slab pressure cumulation over time: the finite width of the Cocos Plate allows the sub-slab pressure to be released around the northern and southern edges of the slab but not in the center. Consequently, the reduced slab dip angle is a result of the enhanced pressure gradient across the slab below western Caribbean, and the eventual slab tear between 85ºW and 93ºW represents the failure of the weak and young subducting plate. This phenomenon is similar to that occurred within the Farallon slab during the mid-Miocene, where the slab tear below Orogen and Nevada led to abrupt surface uplift and upwelling within the mantle wedge (Liu & Stegman, 2012).

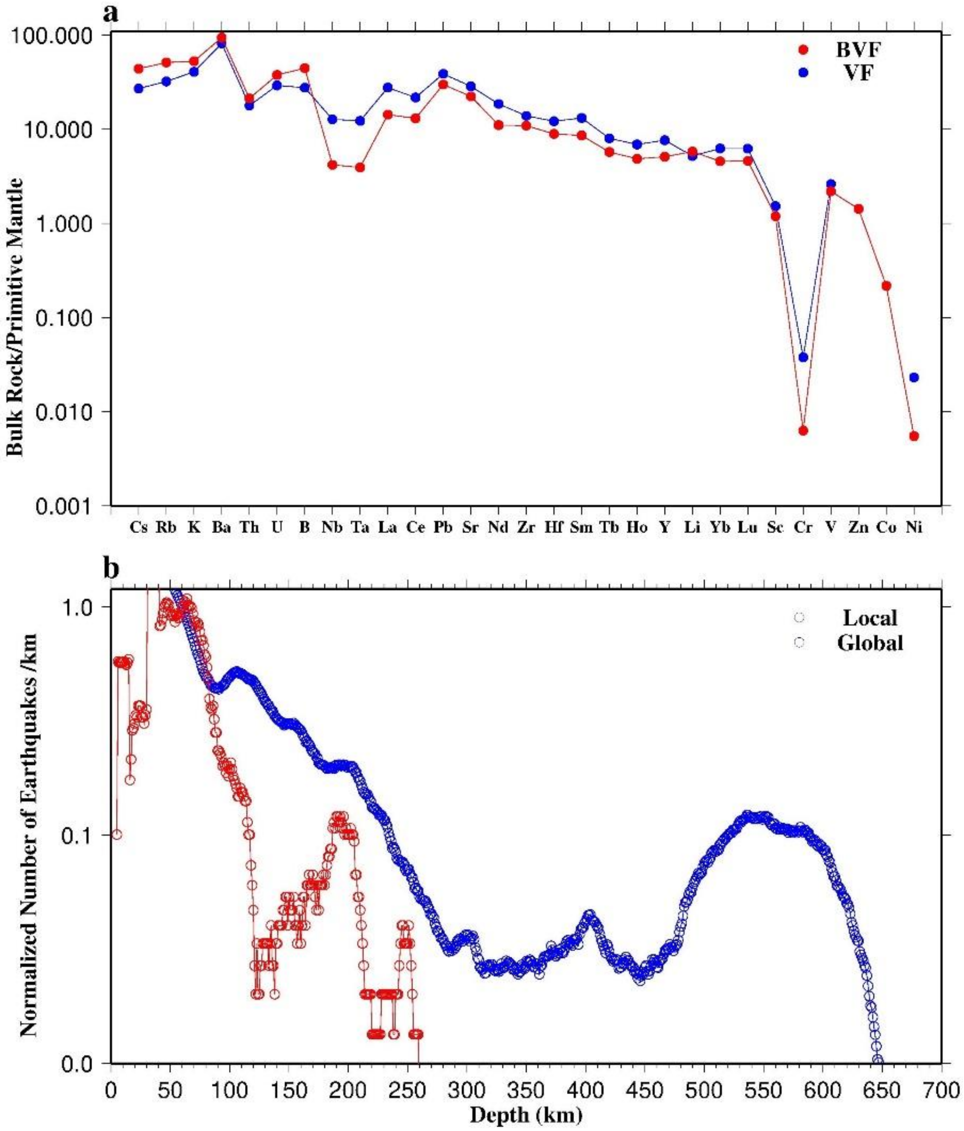

Figure 2. BVF and VF average diagrams. (a). data from Rose and Stoiber (1969), Carr and Pontier (1981), Carr et al. (1984), Walker et al. (1995), Walker et al. (2000), Patino et al. (2000), Walker et al. (2009), and Carr et al. (2014). Primitive mantle values are from McDonough and Sun (1995). (b). Depth variation of the number of M4.0 and greater earthquakes occurred between 2010 and 2022 for northern Central America (red) and the whole Earth (blue). The numbers were normalized by the corresponding value at 60 km depth.

4. ONGOING FRAMENTATION OF THE COCOS SLAB AND ITS GEODYNAMIC IMPLICATIONS

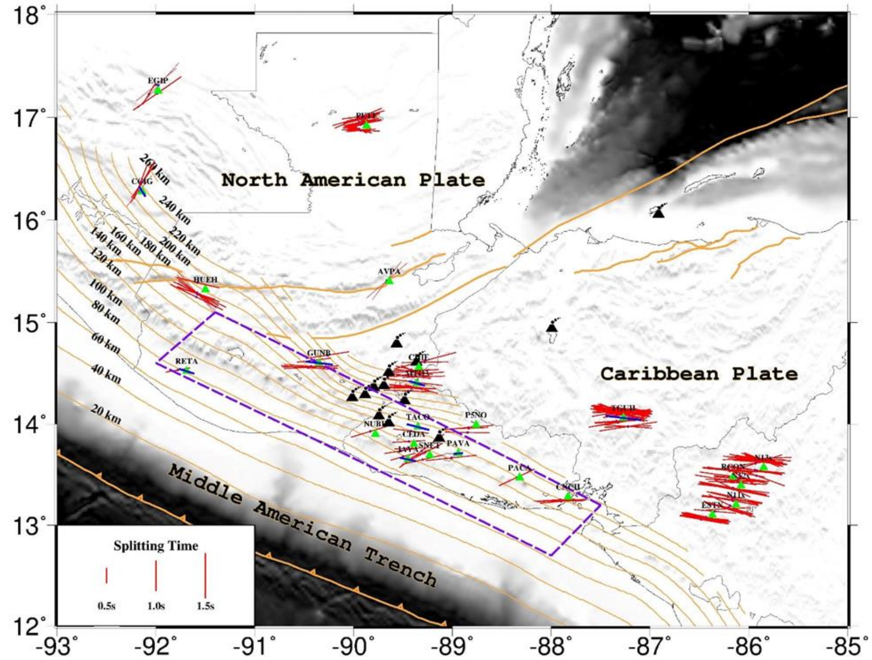

Figure 3. Station-averaged local *S* measurements (black bars) and individual *XKS* measurements (red bars) from this study. The results are plotted at the stations and above the ray-piercing points at 50 km depth, respectively. The area outlined by the dashed lines indicates the approximate extent of the proposed pervious slab.

The realization of a fragmenting Cocos slab could reconcile multiple lines of seemingly contradictory observations. For example, seismic tomography revealed a broken or significantly weakened upper-mantle slab (Rogers et al., 2002; Zhu et al., 2020). In contrast, the existence of intermediate depth earthquakes and VF volcanoes are inconsistent with the existence of a slab window. According to both our simulated present slab geometry (Figure. 4d), inferences of seismic anisotropy (Figure. 3), as well as the area of low gravity anomalies (Supplementary Figure S1), the fragmented portion of the Cocos slab has an along-trench dimension of about 700 km, approximately between

86ºW and 93ºW. In our model, this slab fragmentation starts at about 60 km depth, immediately beneath the lithosphere of the overriding plate, as is confirmed by the observation that the anisotropy-indicated flow systems below ~80 km in the sub-slab region and the mantle wedge show a high degree of continuity (Zhu et al., 2020) (Supplementary Figure S3). The maximum depth of the intensively fractured portion is about 200 km, as this is the depth of suddenly thickened slab thermal structure and increased seismic velocity anomalies (Zhu et al., 2020) (Supplementary Figure S2). This is also the depth below which the earthquake productivity becomes similar to the global subduction zones (Figure 2b).

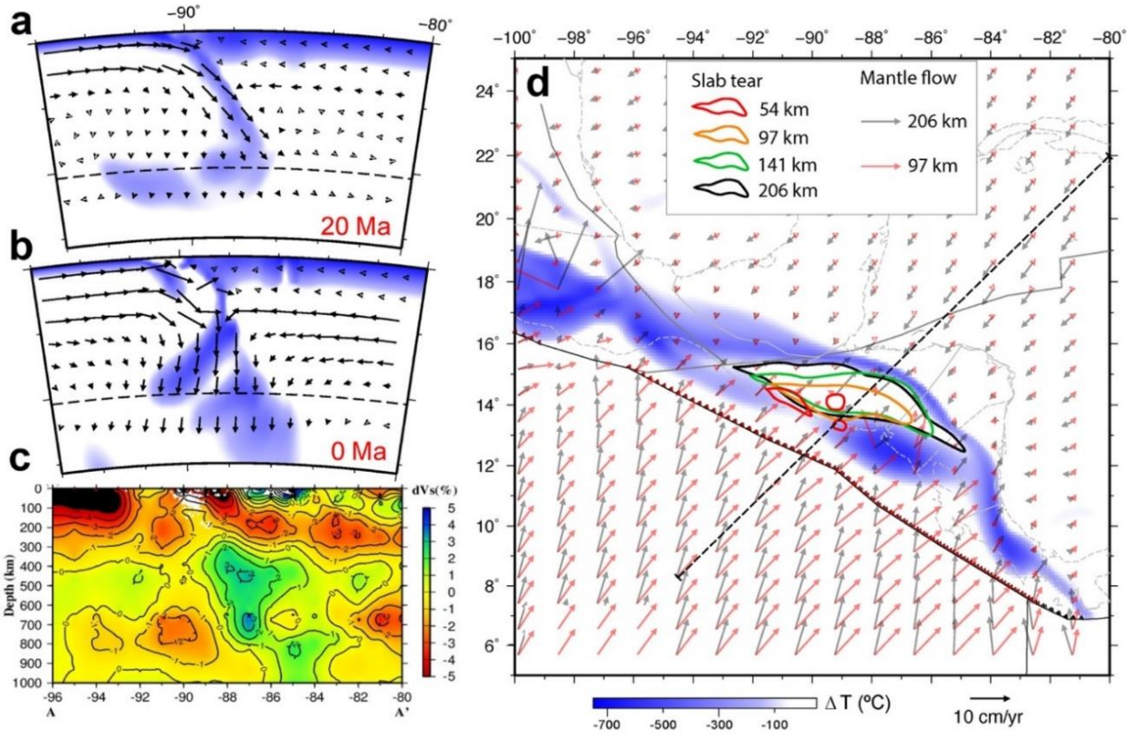

Figure 4. Modeled Cocos slab subduction and mantle flow. Slab evolution at a) 20 Ma and b) present day along the cross section shown in d. c) Seismic image of present slab structure along the same profile (Zhu et al., 2020). d) Map view of present slab geometry, tearing and mantle flow at different depths.

The intensively fractured section of the Cocos slab above 200 km depth is mechanically weaker and warmer than a normal slab due to the strong internal deformation associated with ongoing fragmentation (Figure. 4). Consequently, this slab portion should have a lower earthquake productivity (Figure 2b). Both the reduced mechanical strength and higher temperature of the intensively fractured portion of the slab may also be responsible for the slightly positive velocity anomaly relative to the deeper portion as revealed by seismic tomography (Zhu et al., 2020). This portion of the slab can still carry a sufficient amount of hydrous minerals to produce the VF volcanoes. Meanwhile, the sub-slab mantle material, which has a higher temperature than that in the mantle wedge (Peacocks et al., 2005) and thus is more buoyant, actively migrates upward through the tearing slab hinge to produce the higher-than-normal heat flow, anomalously high elevation, low Bouguer gravity anomalies, and the BVF volcanoes.

5. METHODS

5.1. DATA ACQUISTION

The data set used in this study was obtained from the Incorporated Research Institutions for Seismology (IRIS) Data Management Center (DMC). The data set for shear wave splitting was recorded by 53 broadband seismic stations in 8 different networks in the area of 13-18°N and 85-93°W that recorded data over the period of August 2004 to June 2020. The epicentral distance range used for requesting the *XKS* data is 120°-180° for *PKS,* 90°-180° for *SKKS,* and 84°-180° for *SKS* (Figure S4) *(Gao & Liu, 2009).* The cutoff magnitude is 5.6 for events with a focal depth ≤ 100 km, and for deeper events, the cutoff magnitude is reduced to 5.5. An initial 4-pole 2-pass Butterworth band-pass filter with corner frequencies of 0.04 and 0.5 Hz was applied to all the seismograms to improve the signal-to-noise ratio.

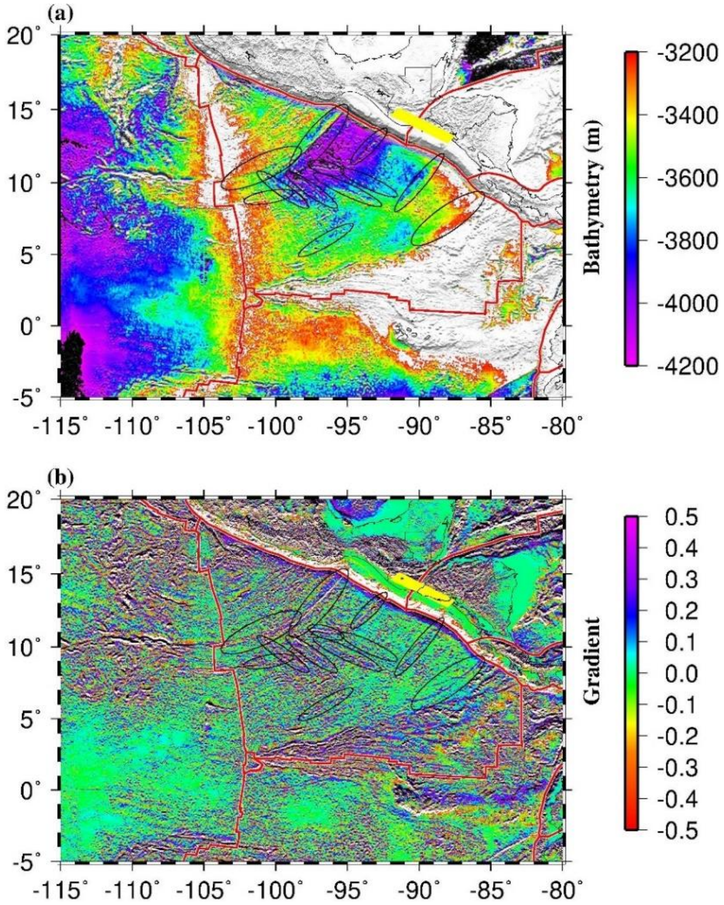

Figure 5. Bathymetry and its gradient of the Cocos plate and surrounding areas. The ellipses highlight major linear features.

5.2. SHEAR WAVE SPLITTING FROM TELESEISMIC WAVES

The splitting parameters were computed using the set of procedures outlined in Liu & Gao (2013) which was based on the transverse component energy minimization technique (Silver & Chan, 1991), and were ranked using a signal-to-noise ratio based ranking system (Liu et al., 2008; Liu & Gao, 2013) into A (outstanding), B (good), C (poor), and N (null) categories. All the automatically measured splitting parameters were manually checked, and if necessary, the beginning and end times of the *XKS* window and the filtering frequencies were adjusted to exclude or reduce non-*XKS* arrivals. Examples of *XKS* measurements are shown in Figure S5. Table S1 shows the results of *XKS* measurements.

5.3. LOCAL S WAVE SPLITING MEASUREMENTS

To provide constraints on the depth distribution of the source of the observed anisotropy using the *XKS* phases, in this study we also analyze the splitting of shear waves from local events. Due to the strong interplay between the local *S* wave and the free surface, only events within the *S* wave window, which is defined by the maximum angle of incidence ($\sin^{-1}(V_s/V_p)$), were used for the splitting analysis (Booth & Crampin, 1985). Given the uncertainty in the velocities beneath each station and to ensure that all the events are in the *S* wave window, in this study only events inside a cone-shaped region with a half vertex angle of 35^o were utilized (Jiang et al., 2021). The epicentral distance range used for data requesting is between 0 and 7°, and the event magnitude is greater than 4.0. All the local *S*-wave seismograms were band-pass filtered in the frequency range of 0.1 to 1.0 Hz. The method of Silver & Chan (1991) was used to simultaneously search for the optimal splitting parameters and the initial (pre-splitting) polarization direction by minimizing the smallest eigenvalue of the corrected covariance matrix. The resultant optimal splitting parameters and initial polarization direction lead to the highest linearity of the corrected particle motion (Figure S5). Note that for both *XKS* and local *S* splitting, station and areal averaged splitting times are calculated using the arithmetic average, while the average fast orientations are computed using the circular (von Mises) statistics (Mardia & Jupp, 2009). The number following the average represents one standard deviation. Table S2 shows the results of local *S* wave splitting measurements.

Table 1. Model parameters

Parameter	Value
Earth's radius, R	6371 km
Mantle thickness, h	2867 km
Mantle density, ρ_m	3340 kg/m^3
Gravitational acceleration, g	9.8 m/s^2
Thermal diffusivity, κ	10^{-6} m^2/s
Thermal expansivity, α	3×10^{-5} K^{-1}
Mantle temperature, T_m	1350ºC
Temperature difference across mantle	1350ºC
Reference viscosity, η_0	10^{21} Pa·s
Rayleigh number, Ra	5.08×10^8
Maximum viscosity cutoff, η_{max}	10^{23} Pa·s
Minimum viscosity cutoff, η_{min}	10^{19} Pa·s
Clapeyron slope at 410 km	4.0 MPa/K
Clapeyron slope at 660 km	-2.0 MPa/K

5.4. GEODYNAMIC MODELING OF SUBDUCTION

We simulate the Cenozoic subduction and mantle flow along the Central American trench by solving thermal-chemical convection based on data-assimilation techniques (Liu and Stegman, 2011; Hu et al., 2016; Peng et al., 2021). We assume that the mantle is incompressible and satisfies the Boussinesq approximation without internal heating. We use the spherical finite element code CitcomS (Zhong et al., 2008) to solve the equations for the conservation of mass, momentum and energy and the advection of chemical particles:

$$\nabla \cdot \vec{u} = 0, \qquad (1)$$

$$-\nabla P + \nabla \cdot [\eta(\nabla \vec{u} + \nabla^T \vec{u})] + (\rho_m \alpha \Delta T + \Delta \rho_c)\vec{g} = 0, \qquad (2)$$

$$\frac{\partial T}{\partial t} + \vec{u} \cdot \nabla T = \kappa \nabla^2 T, \qquad (3)$$

$$\frac{\partial C}{\partial t} + \vec{u} \cdot \nabla C = 0, \qquad (4)$$

where $\vec{u}$ is the mantle velocity, P is the dynamic pressure, η is the dynamic viscosity, ρ_m is the density of the ambient mantle, α is the thermal expansion coefficient, ΔT is the temperature anomaly, $\Delta \rho_c$ is the compositional density anomaly, $\vec{g}$ is the gravitational acceleration, and C is composition. The adopted values of model parameters are listed in Table 1.

The model domain is 130ºW to 40ºW, 15ºS to 45ºN and from the surface to the core-mantle boundary (CMB). The numerical mesh has $513 \times 513 \times 113$ nodes, with spatially uneven resolution. In the horizontal directions, the resolution is 12 km by 18 km in the central 2/3 of the model domain. In the vertical direction, the resolution is ~11 km in the upper mantle and gradually coarsens to 32 km near the CMB. The model duration covers the geological history since 45 Ma.

Boundary conditions: The CMB is assumed to be a free-slip boundary. The surface assimilates velocities that are based on a recent plate reconstruction (Müller et al., 2019). The temperature profile for the oceanic plates is defined with a modified plate model (Liu and Stegman 2011; Hu et al., 2016; Peng et al., 2021). For seafloor age younger than 80 Myr, the temperature profile follows the half-space cooling model, and that of older seafloors has the same profile as the 80 Myr case. The continental plates have an initial steady state geotherm, whose structure subsequently evolves in response to subduction dynamics.

Compositional structure: We utilize 12 chemical compositions to reproduce realistic crustal and mantle processes. Each element contains 35 tracers initially, resulting in 1 billion chemical tracers in total. By solving both thermal and compositional evolution of the system, our model is more capable to reproduce asymmetric subduction and the associated multiple-scale dynamics compared to the pure-thermal simulations commonly used in earlier studies.

Viscosity structure: The model incorporates a 3D Newtonian viscosity structure that depends on depth, temperature, and composition, following

$$\eta = \eta_0(r) \cdot C \cdot exp(\frac{E_\eta(r)}{T+T_\eta(r)} - \frac{E_\eta(r)}{T_m+T_\eta(r)}), \qquad (5)$$

where η is the effective viscosity, $\eta_0(r)$ is the depth-dependent background viscosity, C is the compositional multiplier, $E_\eta(r)$ is the activation energy, $T_\eta(r)$ is the activation temperature, T is temperature and T_m is the background temperature. The reference viscosity is 10^{21} Pa s.

APPENDIX

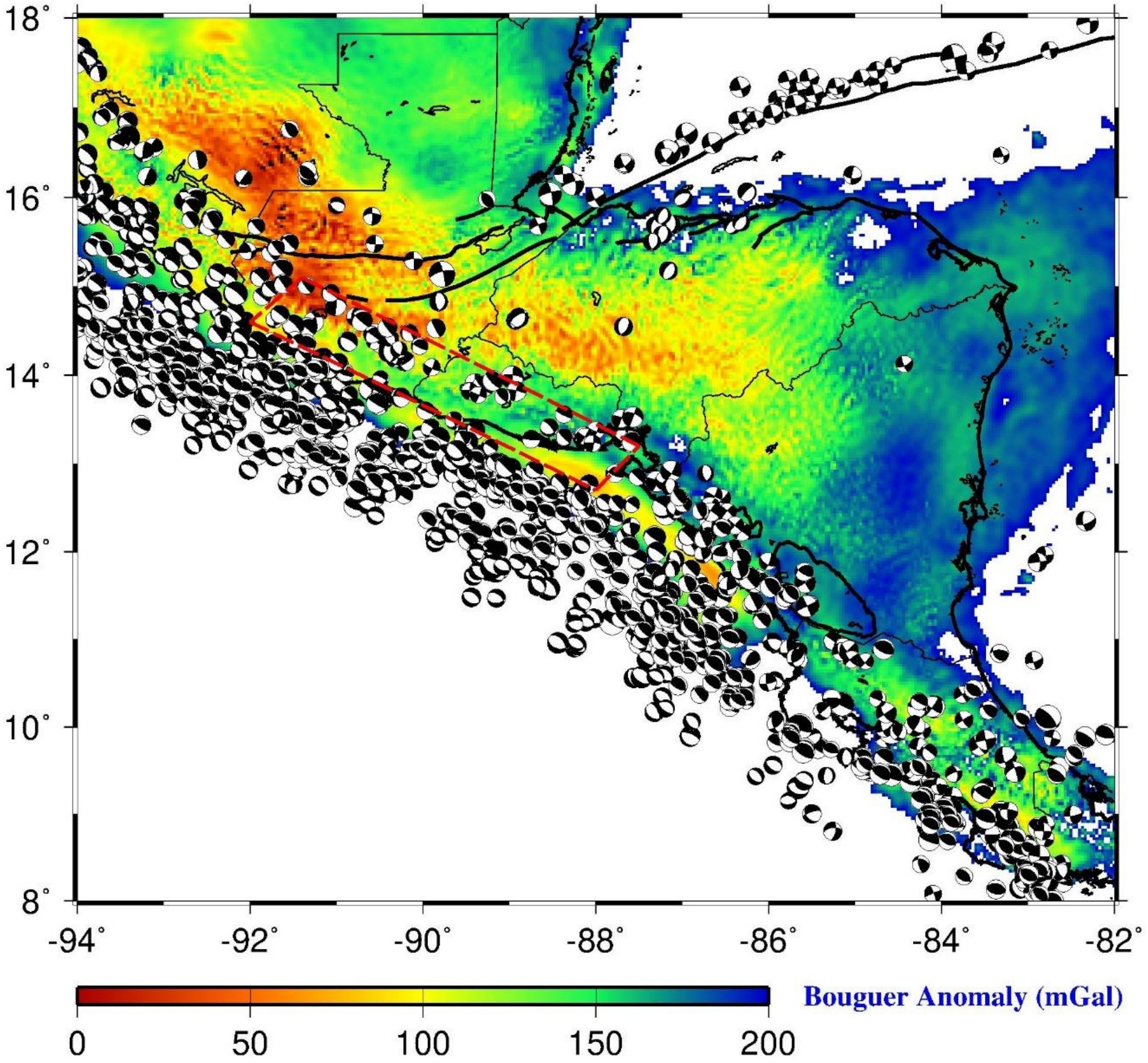

Figure S1. Bouguer gravity anomalies and focal mechanism solutions. The area outlined by the dashed lines indicates the approximate extent of the proposed pervious slab.

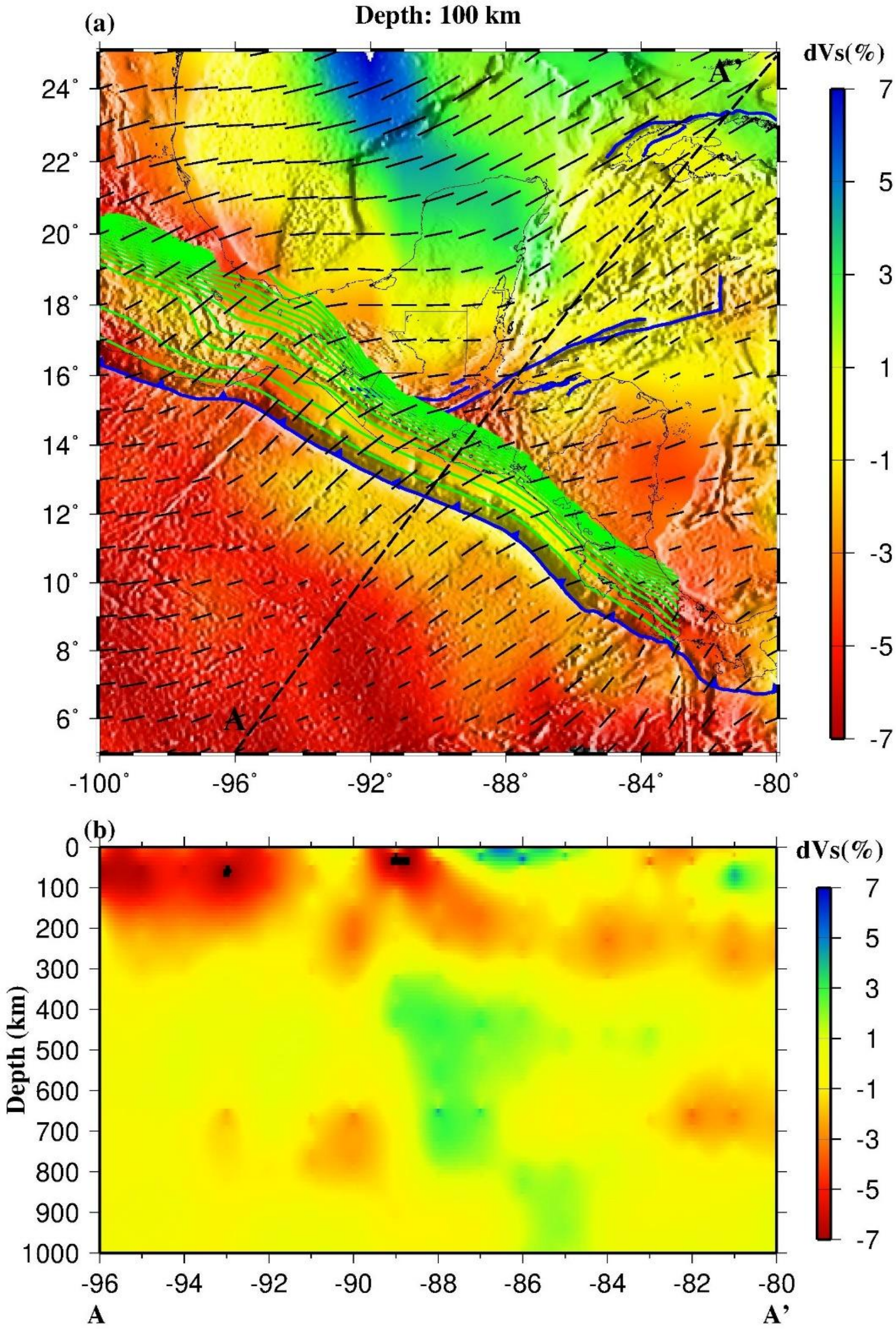

Figure S2. (a) Isotropic S-wavespeed anomalies and azimuthal anisotropy at 100 km deep. (b) S-wavespeed anomalies along Profile A-A' in (a). White stars represent M ≥ 4.0 earthquakes in a 40-km wide band centered at the profile during 1980-2022.

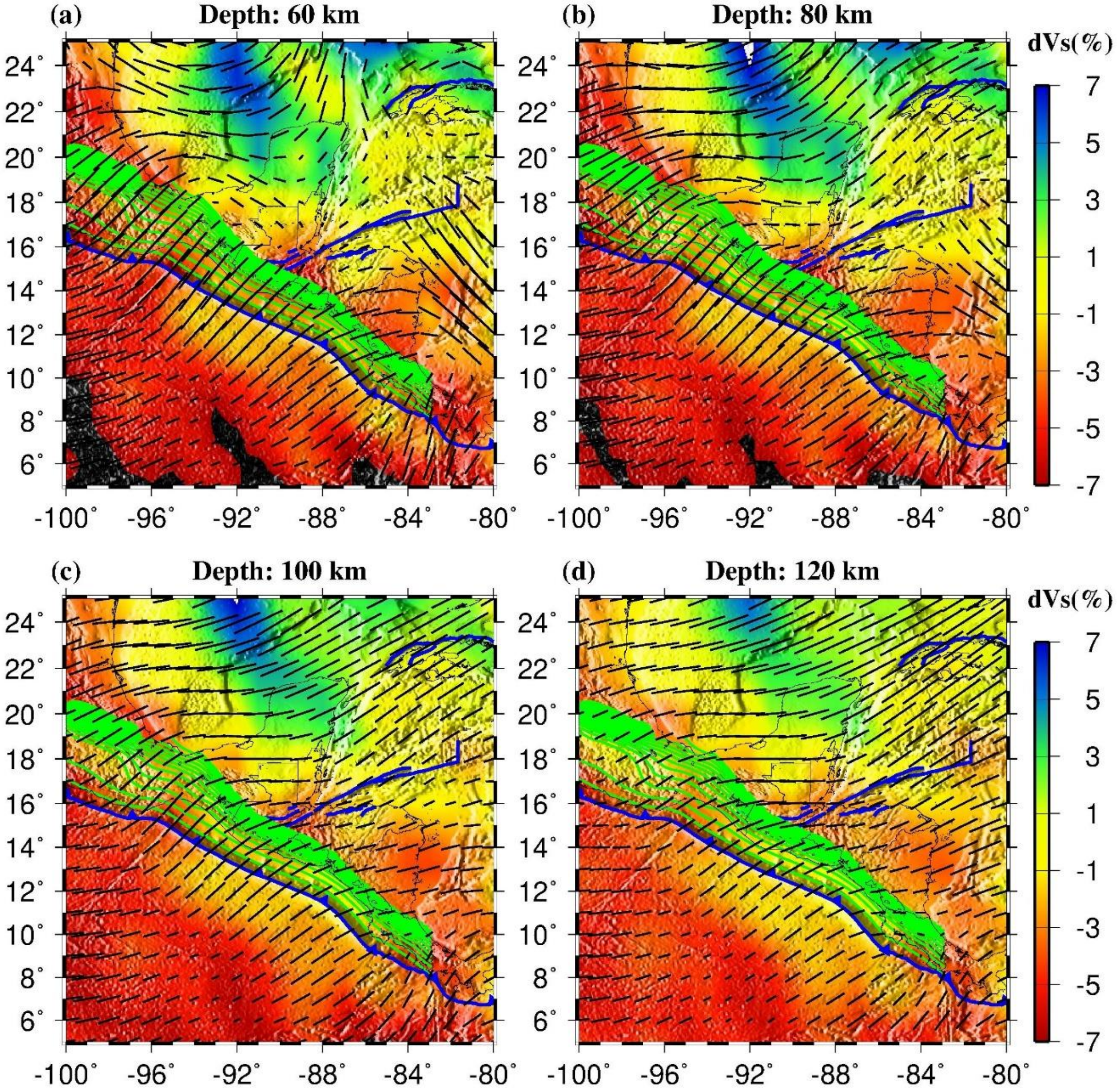

Figure S3. Isotropic S-wavespeed anomalies (background colors) and azimuthal anisotropy (bars) at 4 depths.

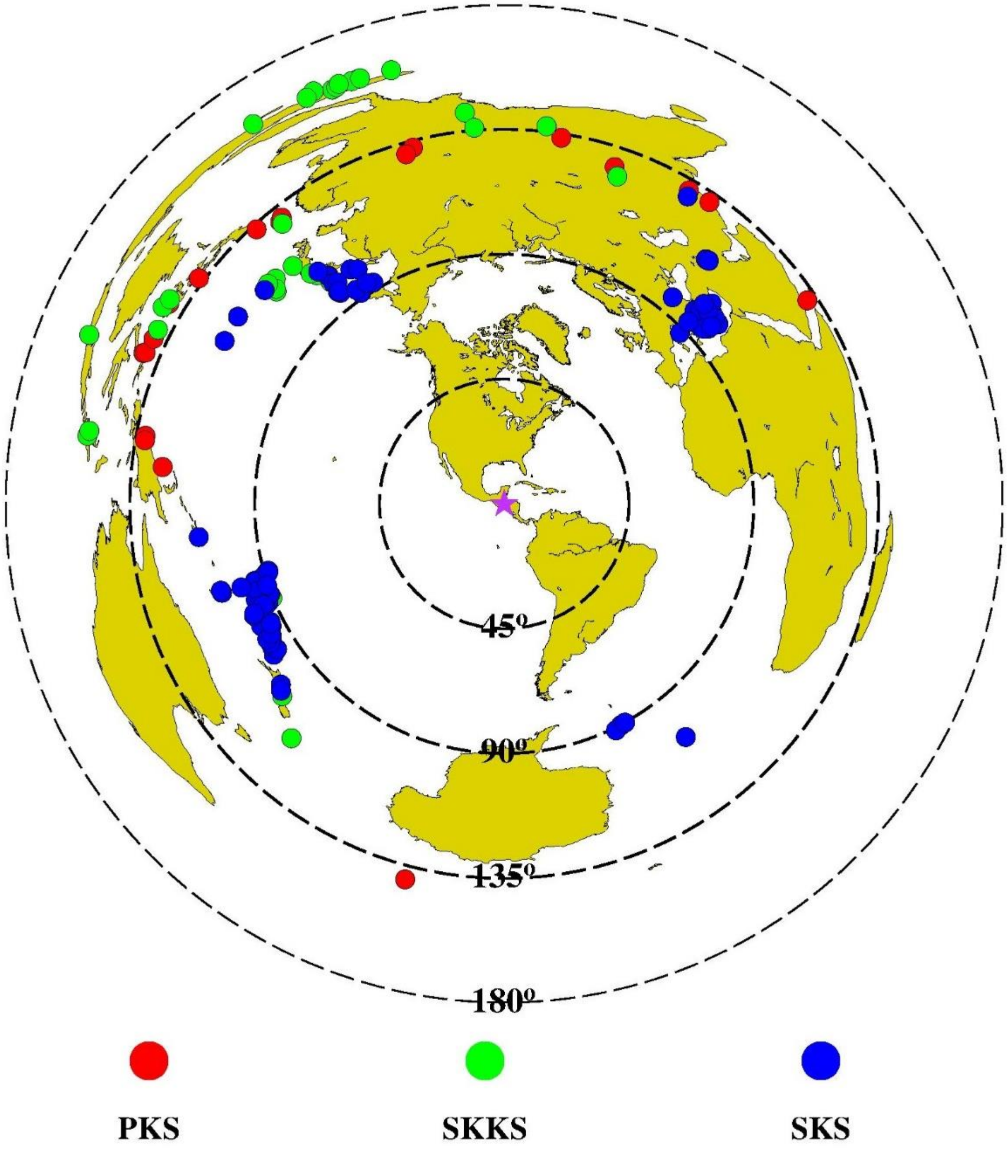

Figure S4. Azimuthal equidistant maps showing the spatial distribution of the events for the 21 PKS, 55 SKK, and 129 SKS measurements.

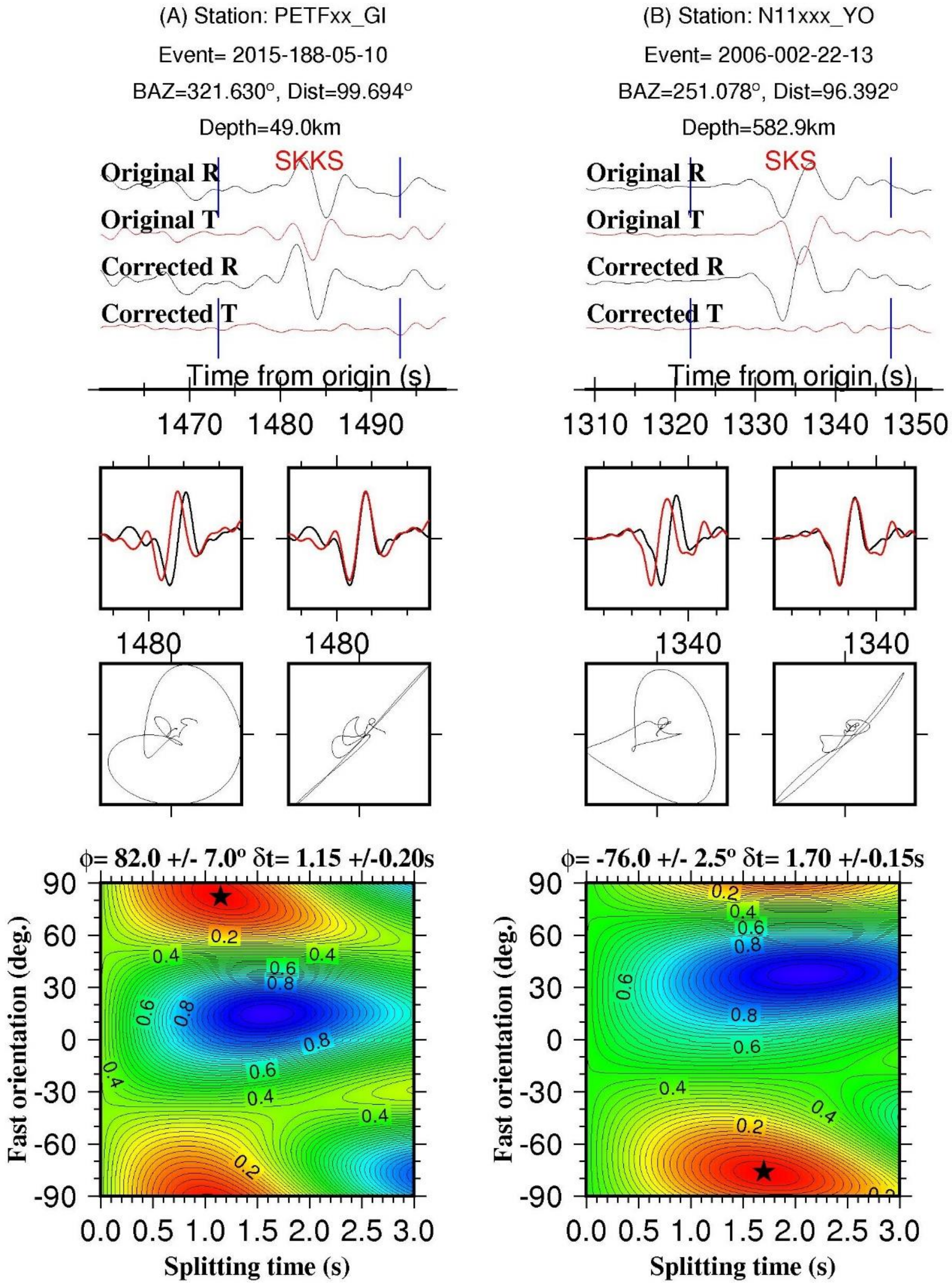

Figure S5. SWS measurements for station PETF (left panels) and N11 (right panels). For each panel, the top plots show the original and corrected radial and transverse components, the middle plots show original and corrected particle motion patterns, and the contour diagram at the bottom shows the energy on the corrected transverse component with the optimal pair of splitting parameter (the black star) corresponding to the minimum energy.

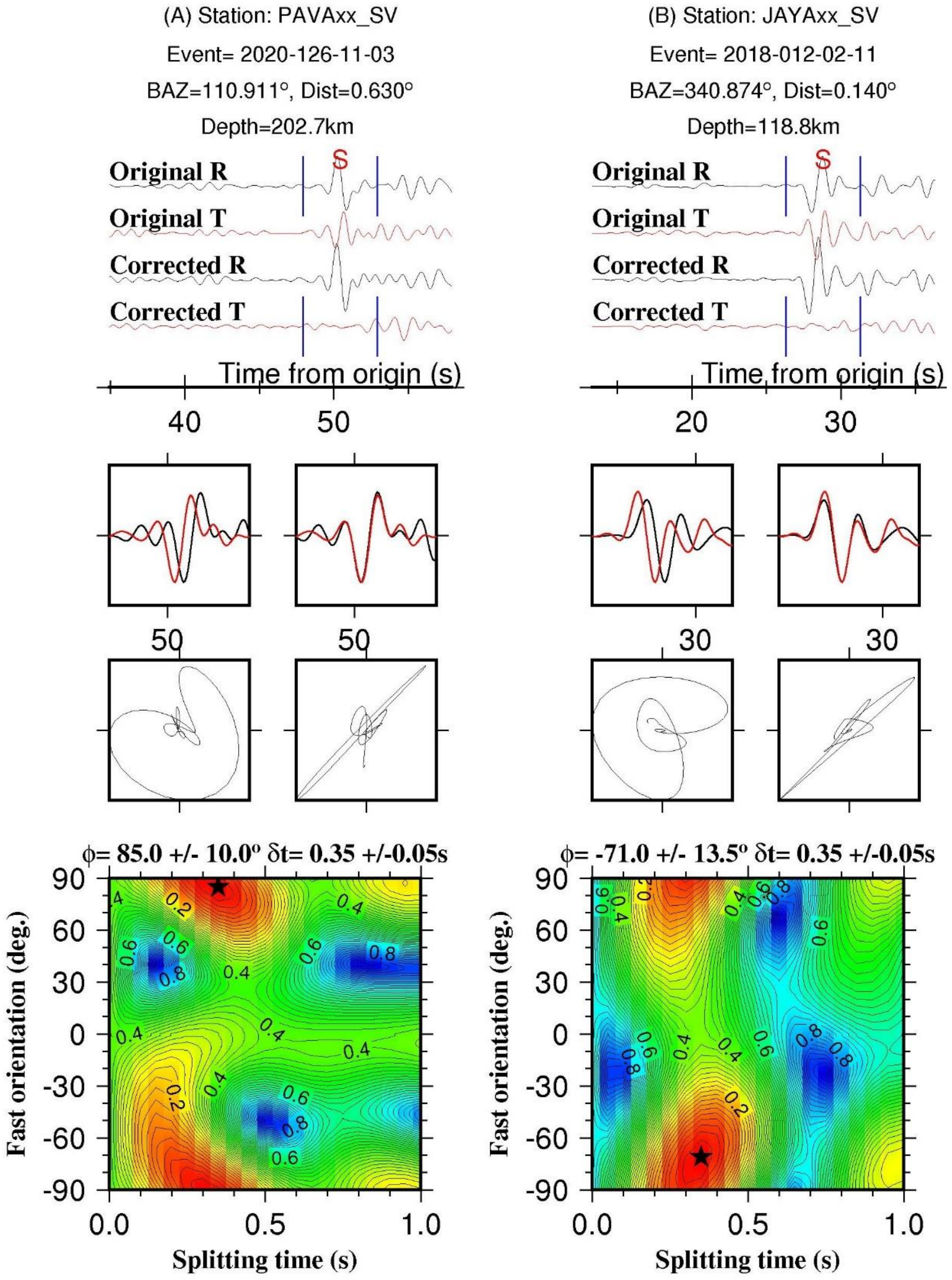

Figure S6. Same as the previous figure but for local *S* wave splitting analyses using data recorded by Station PAVA and JAYA.

Table S1. Station-averaged *XKS* measurements.

name	lon (deg.)	lat (deg.)	phi (deg.)	σ (deg.)	t (sec.)	σ (sec.)	#
AVPA	-89.64	15.40	43.00	6.0	1.70	0.10	2
CCIG	-92.14	16.28	31.28	6.7	1.36	0.09	4
CEDA	-89.39	13.80	87.50	0.5	0.95	0.15	2
CHIE	-89.34	14.56	-86.58	12.4	1.40	0.17	7
CNCH	-87.83	13.28	87.40	1.4	1.40	0.14	5
EGIP	-91.98	17.26	44.82	9.3	1.64	0.29	4
ESTN	-86.37	13.10	-80.30	3.1	1.50	0.04	10
GUNB	-90.35	14.60	88.00	5.0	1.64	0.12	6
HUEH	-91.50	15.32	-59.56	10.4	1.65	0.06	11
JAYA	-89.45	13.65	77.50	3.5	0.97	0.12	2
MTO3	-89.36	14.40	-86.19	5.2	1.49	0.07	11
N11	-86.13	13.20	-77.45	7.4	1.70	0.06	11
N12	-86.08	13.39	-80.15	8.1	1.85	0.12	14
N13	-85.85	13.57	-82.36	8.8	1.59	0.07	26
NUBE	-89.78	13.90	73.00	11.5	1.35	0.30	1
P5NO	-88.76	13.99	88.00	2.5	1.48	0.10	3
PACA	-88.32	13.47	65.00	2.0	1.30	0.10	1
PAVA	-88.94	13.71	84.00	4.0	1.70	0.23	1
PETF	-89.87	16.92	-77.20	7.9	0.80	0.10	24
RCON	-86.16	13.48	-83.40	2.4	1.82	0.09	5
RETA	-91.69	14.52	80.00	14.0	0.80	1.75	1
SNET	-89.23	13.69	64.74	8.7	1.40	0.17	4
TACO	-89.35	13.97	-83.00	11.5	1.20	0.38	1
TGUH	-87.27	14.06	-86.64	7.5	1.48	0.03	49

Table S2. Station-averaged local *S* measurements.

name	lon (deg.)	lat (deg.)	phi (deg.)	σ (deg.)	t (sec.)	σ (sec.)	#
CCIG	-92.14	16.28	-32.00	11.5	0.35	0.35	1
GUNB	-90.35	14.60	-83.33	2.1	0.87	0.13	3
JAYA	-89.45	13.65	-77.69	6.8	0.50	0.10	4
MTO3	-89.36	14.40	-74.50	0.5	0.50	0.00	2
PAVA	-88.94	13.71	85.00	17.5	0.25	0.08	1
RETA	-91.69	14.52	-72.59	10.0	0.48	0.12	7
TACO	-89.35	13.97	-75.50	8.6	0.72	0.33	2
TGUH	-87.27	14.06	-83.00	4.5	1.14	0.04	8

REFERENCES

Abt, D. L., Fischer, K. M., Abers, G. A., Protti, M., González, V., & Strauch, W. (2010). Constraints on upper mantle anisotropy surrounding the Cocos slab from SK (K) S splitting. Journal of Geophysical Research: Solid Earth, 115(B6). https://doi.org/10.1029/2009JB006710

Abt, D. L., Fischer, K. M., Abers, G. A., Strauch, W., Protti, J. M., & González, V. (2009). Shear wave anisotropy beneath Nicaragua and Costa Rica: Implications for flow in the mantle wedge. Geochemistry, Geophysics, Geosystems, 10(5). https://doi.org/10.1029/2009GC002375

Ando, M., Ishikawa, Y., & Yamazaki, F. (1983). Shear wave polarization anisotropy in the upper mantle beneath Honshu, Japan. Journal of Geophysical Research: Solid Earth, 88(B7), 5850-5864. https://doi.org/10.1029/JB088iB07p05850

Bernal-López, L. A., Garibaldi, B. R., Soto, G. L., Valenzuela, R. W., & Escudero, C. R. (2016). Seismic anisotropy and mantle flow driven by the Cocos slab under southern Mexico. Pure and Applied Geophysics, 173(10-11), 3373-3393. https://doi.org/10.1007/s00024-015-1214-7

Bina, C. R., & Helffrich, G. (1994). Phase transition Clapeyron slopes and transition zone seismic discontinuity topography. Journal of Geophysical Research: Solid Earth, 99(B8), 15853-15860. https://doi.org/10.1029/94JB00462

Castellanos, J., Pérez-Campos, X., Valenzuela, R., Husker, A., & Ferrari, L. (2017). Crust and upper-mantle seismic anisotropy variations from the coast to inland in central and Southern Mexico. Geophysical Journal International, 210(1), 360-374. https://doi.org/10.1093/gji/ggx174

Fei, Y., Van Orman, J., Li, J., Van Westrenen, W., Sanloup, C., Minarik, W., ... & Funakoshi, K.I. (2004). Experimentally determined postspinel transformation boundary in Mg2SiO4 using MgO as an internal pressure standard and its geophysical implications. Journal of Geophysical Research: Solid Earth, 109(B2). https://doi.org/10.1029/2003JB002562

Helffrich, G. (2000). Topography of the transition zone seismic discontinuities. Reviews of Geophysics, 38(1), 141-158. https://doi.org/10.1029/1999RG000060

Herrstrom, E. A., Reagan, M. K., & Morris, J. D. (1995). Variations in lava composition associated with flow of asthenosphere beneath southern Central America. Geology, 23(7), 617-620. https://doi.org/10.1130/0091-7613(1995)023<0617:VILCAW>2.3.CO;2

Hess, H. H. (1964). Seismic anisotropy of the uppermost mantle under oceans. Nature, 203(4945), 629-631. https://doi.org/10.1038/203629a0

Hoernle, K., Abt, D. L., Fischer, K. M., Nichols, H., Hauff, F., Abers, G. A., ... & Strauch, W. (2008). Arc-parallel flow in the mantle wedge beneath Costa Rica and Nicaragua. Nature, 451(7182), 1094. https://doi.org/10.1038/nature06550

Ito, E., & Katsura, T. (1989). A temperature profile of the mantle transition zone. Geophysical Research Letters, 16(5), 425-428. https://doi.org/10.1029/GL016i005p00425

Kennett, B. L. N., & Engdahl, E. R. (1991). Traveltimes for global earthquake location and phase identification. Geophysical Journal International, 105(2), 429-465. https://doi.org/10.1111/j.1365-246X.1991.tb06724.x

Johnston, S. T., & Thorkelson, D. J. (1997). Cocos-Nazca slab window beneath central America. Earth and Planetary Science Letters, 146(3-4), 465-474. https://doi.org/10.1016/S0012-821X(96)00242-7

Jung, H., & Karato, S. I. (2001). Water-induced fabric transitions in olivine. Science, 293(5534), 1460-1463. DOI: 10.1126/science.1062235

Kong, F., Gao, S. S., Liu, K. H., Zhang, J., & Li, J. (2020). Seismic anisotropy and mantle flow in the Sumatra subduction zone constrained by shear wave splitting and receiver function analyses. Geochemistry, Geophysics, Geosystems, 21(2), e2019GC008766. https://doi.org/10.1029/2019GC008766

Kong, F., et al., 2022, Metastable olivine within oceanic lithosphere in the uppermost lower mantle beneath the eastern United States: Geology, v. XX, p. XXX–XXX, https://doi.org/10.1130/G49879.1

Lawrence, J. F., & Shearer, P. M. (2006). A global study of transition zone thickness using receiver functions. Journal of Geophysical Research: Solid Earth, 111(B6). https://doi.org/10.1029/2005JB003973

León Soto, G., & Valenzuela, R. W. (2013). Corner flow in the Isthmus of Tehuantepec, Mexico inferred from anisotropy measurements using local intraslab earthquakes. Geophysical Journal International, 195(2), 1230-1238. https://doi.org/10.1093/gji/ggt291

Levin, V., Elkington, S., Bourke, J., Arroyo, I., & Linkimer, L. (2021). Seismic anisotropy in southern Costa Rica confirms upper mantle flow from the Pacific to the Caribbean. Geology, 49(1), 8-12. https://doi.org/10.1130/G47826.1

Li, C., van der Hilst, R. D., Engdahl, E. R., & Burdick, S. (2008). A new global model for P wave speed variations in Earth's mantle. Geochemistry, Geophysics, Geosystems, 9(5).https://doi.org/10.1029/2007GC001806

Liu, L. and D.R. Stegman (2011), Segmentation of Farallon slab, Earth Planet. Sci. Lett. 311, 1-10.

Liu, L. and D.R. Stegman (2012), Origin of Columbia River flood basalt controlled by propagating rupture of the Farallon slab, Nature, 482, 386-389.

Litasov, K. D., Ohtani, E., Sano, A., Suzuki, A., & Funakoshi, K. (2005). Wet subduction versus cold subduction. Geophysical Research Letters, 32(13). https://doi.org/10.1029/2005GL022921

Long, M. D., & Becker, T. W. (2010). Mantle dynamics and seismic anisotropy. Earth and Planetary Science Letters, 297(3-4), 341-354. https://doi.org/10.1016/j.epsl.2010.06.036

Long, M. D., & Silver, P. G. (2008). The subduction zone flow field from seismic anisotropy: A global view. science, 319(5861), 315-318. DOI: 10.1126/science.1150809

Long, M. D., & Silver, P. G. (2009). Mantle flow in subduction systems: The subslab flow field and implications for mantle dynamics. Journal of Geophysical Research: Solid Earth, 114(B10). https://doi.org/10.1029/2008JB006200

Lyon-Caen, H., Barrier, E., Lasserre, C., Franco, A., Arzu, I., Chiquin, L., ... & Luna, J. (2006). Kinematics of the North American–Caribbean-Cocos plates in Central America from new GPS measurements across the Polochic-Motagua fault system. Geophysical Research Letters, 33(19). https://doi.org/10.1029/2006GL027694

Peacock, S. M., van Keken, P. E., Holloway, S. D., Hacker, B. R., Abers, G. A., & Fergason, R. L. (2005). Thermal structure of the Costa Rica–Nicaragua subduction zone. Physics of the Earth and Planetary Interiors, 149(1-2), 187-200.https://doi.org/10.1016/j.pepi.2004.08.030

Ringwood, A. E. (1975). Composition and Petrology of the Earth's Mantle. MacGraw-Hill, 618.

Rogers, R. D., Kárason, H., & van der Hilst, R. D. (2002). Epeirogenic uplift above a detached slab in northern Central America. Geology, 30(11), 1031-1034. https://doi.org/10.1130/0091-7613(2002)030<1031:EUAADS>2.0.CO;2

Russo, R. M., & Silver, P. G. (1994). Trench-parallel flow beneath the Nazca plate from seismic anisotropy. Science, 263(5150), 1105-1111. DOI: 10.1126/science.263.5150.1105

Silver, P. G. (1996). Seismic anisotropy beneath the continents: Probing the depths of geology. Annual review of earth and planetary sciences, 24(1), 385-432. https://doi.org/10.1146/annurev.earth.24.1.385

Silver, P. G., & Chan, W. W. (1991). Shear wave splitting and subcontinental mantle deformation. Journal of Geophysical Research: Solid Earth, 96(B10), 16429-16454.https://doi.org/10.1029/91JB00899

Sun, M., Yu, Y., Gao, S. S., & Liu, K. H. (2022). Stagnation and tearing of the subducting northwest Pacific slab. Geology. https://doi.org/10.1130/G49862.1

Stoiber, R., & Carr, M. (1973). Quaternary volcanic and tectonic segmentation of Central America. Bulletin Volcanologique, 37(3), 304-325. https://doi.org/10.1007/BF02597631

Tschauner, O., Ma, C., Beckett, J. R., Prescher, C., Prakapenka, V. B., & Rossman, G. R. (2014). Discovery of bridgmanite, the most abundant mineral in Earth, in a shocked meteorite. Science, 346(6213), 1100-1102. DOI: 10.1126/science.1259369

van Benthem, S. A., Valenzuela, R. W., & Ponce, G. J. (2013a). Measurements of upper mantle shear wave anisotropy from a permanent network in southern Mexico. Geofísica internacional, 52(4), 385-402. https://doi.org/10.1016/S0016-7169(13)71485-5

van Benthem, S., Govers, R., Spakman, W., & Wortel, R. (2013b). Tectonic evolution and mantle structure of the Caribbean. Journal of Geophysical Research: Solid Earth, 118(6), 3019-3036. https://doi.org/10.1002/jgrb.50235

Van der Meer, D. G., Van Hinsbergen, D. J., & Spakman, W. (2018). Atlas of the underworld: Slab remnants in the mantle, their sinking history, and a new outlook on lower mantle viscosity. Tectonophysics, 723, 309-448. https://doi.org/10.1016/j.tecto.2017.10.004

Walker, J. A., Carr, M. J., Patino, L. C., Johnson, C. M., Feigenson, M. D., & Ward, R. L. (1995). Abrupt change in magma generation processes across the Central American arc in southeastern Guatemala: Flux-dominated melting near the base of the wedge to decompression melting near the top of the wedge. Contributions to Mineralogy and Petrology, 120(3), 378-390. https://doi.org/10.1007/BF00306515

Walker, J. A., Patino, L. C., Cameron, B. I., & Carr, M. J. (2000). Petrogenetic insights provided by compositional transects across the Central American arc: Southeastern Guatemala and Honduras. Journal of Geophysical Research: Solid Earth, 105(B8), 18949-18963. https://doi.org/10.1029/2000JB900173

Wortel, M. J. R., & Spakman, W. (2000). Subduction and slab detachment in the Mediterranean-Carpathian region. Science, 290(5498), 1910-1917. DOI: 10.1126/science.290.5498.1910

Yang, Y., Gao, S. S., Liu, K. H., Kong, F., & Fu, X. (2021). Mantle Flow in the Vicinity of the Eastern Edge of the Pacific-Yakutat Slab: Constraints from Shear Wave Splitting Analyses. Journal of Geophysical Research: Solid Earth, e2021JB022354. https://doi.org/10.1029/2021JB022354

Zhang, S., & Karato, S. I. (1995). Lattice preferred orientation of olivine aggregates deformed in simple shear. Nature, 375(6534), 774. https://doi.org/10.1038/375774a0

Zhou, Q., J. Hu, L. Liu, T. Chaparro, D.R. Stegman, M. Faccenda (2018), Western U.S. seismic anisotropy revealing complex mantle dynamics, Earth Planet. Sci. Lett., 500, 156-167.

II. RECEIVER FUNCTION INVESTIGATION OF MANTLE TRANSITION ZONE DISCONTINUITIES BENEATH EASTERN CARIBBEAN

ABSTRACT

To investigate the effects of plate subduction on the thermal structure of the mantle transition zone (MTZ), we stack over 8000 P-to-S receiver functions from 1901 events recorded by 115 stations in the vicinity of eastern Caribbean under the non-plane way assumption to image the 410 and 660 km discontinuities and map the spatial variation of the thickness of the MTZ. The receiver functions are grouped into circular bins with a radius of 1o and moveout corrected using the 1-D IASP91 Earth model prior to stacking. After wavespeed correction based on three earth models US32, TX2019slab, and UU-P07, spatially variable MTZ thickness is revealed, which can be attributed to subducted cold slabs and thermal upwelling along slab gaps. In the Lesser Antilles subduction zone, a thinner than normal MTZ is revealed and is attributable to mantle upwelling beneath the slab gap in this area. The MTZ thinning is mostly caused by an uplifted 660 km discontinuity, suggesting that the thermal upwelling may originate from the lower mantle. The uplifted 410 km discontinuity and depressed 660 km discontinuity in the southern Lesser Antilles Subduction Zone probably indicate the existence of cold slabs.

1. INTRODUCTION

The Caribbean (CA) Plate is surrounded by the North American (NA) Plate to the north, the South American (SA) Plate to the east and south, the Nazca (NZ) Plate to the southwest, and the Cocos (CO) Plate to the west (Figure 1A). The interaction among the plates resulted in a complex evolutionary history of the CA Plate and surrounding plate boundary zones, whose origin has been described by two major models. The ‘Pacific’ model proposes that the CA Plate originated within the Farallon Plate, and as a result of the subduction of the Farallon Plate, the CA Plate later moved to its present position between the two American Plates (Pindell & Barrett, 1990). In contrast, the ‘Intra-Americans’ model suggests that the CA Plate originated between the NA and SA Plates as the results of fragmentation of the American Plate (Meschede & Frisch, 1998). From the Late Cretaceous until the Eocene, the Atlantic lithosphere subducted westward beneath the eastern boundary of the CA Plate. This subduction created the Great Arc of the Caribbean, which is a remnant arc and is currently the Great Antilles (Laurencin et al., 2018). The subduction also created an active arc, the Lesser Antilles arc (Laurencin et al., 2018). The west-dipping subduction of the Atlantic lithosphere beneath the Lesser Antilles continues from the Eocene until the present (van Benethem et al., 2013).

Active and passive source seismic and earthquake focal mechanism studies (Ten Brink, 2005; Harris et al., 2018; Meighan et al., 2013) indicate a possible slab gap near Puerto Rico in the northern Lesser Antilles, approximately centered at 68oW (Figure 1A). The V-shaped gap has a maximum width of ~100 km at the top and extends to a depth of ~ 300 km on the tomographic images (Harris et al., 2018). The presence of this slab gap is indicated by sudden changes in fast orientation of SKS splitting analysis (Schlaphorst et al., 2017), but is not imaged by some of the other tomography studies (van Benethem et al., 2013). A second slab gap, approximately centered at ~ 14oN and extending to at least 200 km depth, has been proposed to exist between the NA and SA Plates (Figure 1A), on the basis of the absence of the Wadati-Benioff Zone (Wadge & Shepherd, 1984), P-wave tomography models (van Benethem et al., 2013; Harris et al., 2018) and seismic anisotropy (Schlaphorst et al., 2017). Due to the diminishing resolution with the depth of the tomographic images, whether the gaps have extended to MTZ remains unclear.

Numerous previous studies have demonstrated that the topography of 410 km and 660 km discontinuities (hereafter referred to as d410 and d660), which define the top and bottom of the MTZ (Shearer & Flanagan, 1999) can be used to constrain the depth extent of subducted cold slabs and high temperature anomalies (Collier & Helffrich, 1997; Li et al., 1998; Liu et al, 2003; Dahm et al., 2017; Yu et al., 2017; Sun et al., 2018, Kong et al., 2020). The d410 and d660 are well established in most global models and are associated with a globally mean MTZ thickness of 250 km (Kennett & Engdahl, 1991). The MTZ discontinuities represent the mineral phase transitions from olivine to wadsleyite at the d410 and from spinel to bridgmanite at the d660 (Ringwood, 1975; Ito & Katsura, 1989; Tschauner et al. 2014). The phase transitions have a close relationship with the temperature and pressure, which can be characterized by the Clapeyron slope, and mineral physical experiments have indicated that the d410 and d660 have positive and negative Clapeyron slopes, respectively (Bina & Helffrich, 1994; Helffrich, 2000; Fei et al., 2004). Thus, a thicker MTZ can be expected in colder regions (e.g. subducted cold slabs) in the MTZ caused by an uplifted d410 and a depressed d660, whereas in hotter areas (e.g. thermal upwelling), a depressed d410 and an uplifted d660 will lead to a thinner MTZ (Ringwood, 1975; Ito & Katsura, 1989; Helffrich, 2000). In addition to thermal anomalies, the existence of water in the MTZ has similar effects as low temperature, which can induce a thicker MTZ (Litasov et al., 2005).

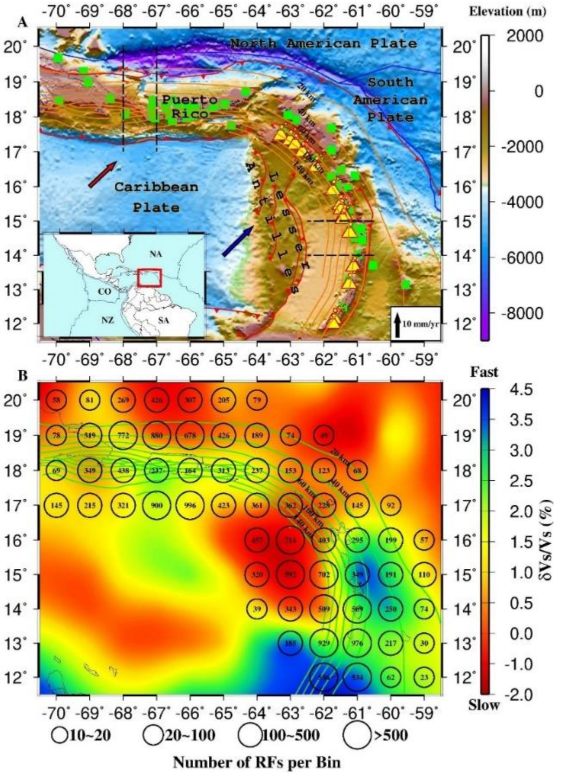

Figure 1. A topographic basemap showing the tectonic setting in eastern Caribbean. The red arrows represent the plate motion of the North American plate relative to the Caribbean Plate and the blue arrows show the plate motion of South American Plate relative to the Caribbean Plate based on the NNR-MORVEL56 model (Argus et al., 2011). The orange lines are the contours of the slab (Hayes, et al., 2018). The green squares are the stations used in this study and the yellow triangles are the volcanoes. The dashed black lines mark the possible location of the slab gaps based on the seismic tomography model of Harris et al. (2018). The inset map shows the location of the study area. NA: North American Plate; SA: South American Plate; NZ: Nazca Plate; CO: Cocos Plate. (B) S wave tomography map showing S-wave velocity variations in the depth of 150 km in the US32 model (Zhu et al., 2020). The purple circles show the location of radius = 1° circular bins. The sizes of circles represent the numbers of the RFs per bin. The green lines represent the contours of the depth of slabs using model Slab 2.0 (Hayes et al., 2018).

To our knowledge, no regional-scale MTZ studies have been conducted for the entire study area, and none of the global MTZ discontinuity studies (e.g., Lawrence & Shearer, 2006) using receiver functions (RFs) has used stations in this area. In this study, we use RFs to image the 410 and 660 km discontinuities and map the spatial variation of the thickness of the MTZ, for purpose of detecting the existence and spatial distribution of subducted slabs and mantle upwelling in eastern Caribbean.

2. DATA AND METHOD

All the three-component broadband data used in this study were obtained from the Incorporated Research Institutions for Seismology (IRIS) Data Management Center (DMC). The data set was recorded by 163 stations from mid-1993 to mid-2022 in the area of 12°N to 20°N, and 59°E to 70°E. The epicentral distances range from 30° to 100°. The cut-off magnitude (Mc) for data is dependent on the empirical equation $Mc = 5.2 + (\Delta -30°) / (180.0-30°) – D / 700.0$, where Δ is the epicentral distance in degree, and D is the focal depth in kilometer (Liu & Gao, 2010). The data processing procedure and parameters used in the study are mostly the same as those used in Gao and Liu (2014a) and are briefly described below.

The original seismograms were filtered with a four-pole and two-pass Bessel filter in the frequency band of 0.02-0.2 Hz. Filtered seismograms with a signal-to-noise ratio (S/N) of 4.0 or greater on the vertical component were assessed using the method of Gao & Liu (2014), and the high S/N seismograms were then converted into radial RFs by deconvolving the vertical from the radial components following the frequency-domain water level deconvolution procedure (Langston, 1979; Ammon, 1991). A total of 8852 high-quality RFs recorded by 115 stations from 1901 events (Figure S1) were used in the study.

The study area is divided into overlapped circular bins with a radius of 1°, which is approximately the radius of the first Fresnel zone at the MTZ depth, and the distance between the center of neighboring bins is also 1°. For each bin, we moveout corrected the RFs with ray-piercing points calculated at the mid of the MTZ (535 km depth) based on the 1-D IASP91 Earth model (Kennett & Engdahl, 1991) and stacked to form depth series in the depth range of 300-800 km under the non-plane wave assumption (Gao & Liu, 2014). To ensure reliability, bins with less than 10 RFs are not used in the study (Figure 3). The mean and standard deviation of the MTZ discontinuity depth and MTZ thickness were computed by applying a bootstrap resampling procedure with 50 resampling iterations (Efron & Tibshirani, 1986; Liu et al., 2003) in the study.

Due to the fact that the RFs were moveout corrected based on the 1-D IASP91 Earth model, the resulting MTZ discontinuity depths are apparent instead of true depths. In this study, we use three wavespeed models, including TX2019slab (Lu et al., 2019), UU-P07 (Amaru, 2007), and US32 (Zhu et al., 2020), which is a global model for P- and S-waves, a global P-wave model and a regional S-wave model, respectively, to correct the apparent depths.

To perform the correction, the mean P- and S-wavespeeds were calculated in each of the radius = 1° circular bins for every 10 km thick layer for the depth range of 0-790 km and were imported to obtain the true depths for the entire study area. For models with only Vp (Vs), we assume an optimal γ factor to find the corresponding Vs (Vp) anomaly for a given depth, and a γ of 1.85 is used in this study. As demonstrated below, the resulting corrected d410 and d660 depths and especially the corrected MTZ thickness using three model are similar to each other, so we take the average values of three models as our final corrected depths.

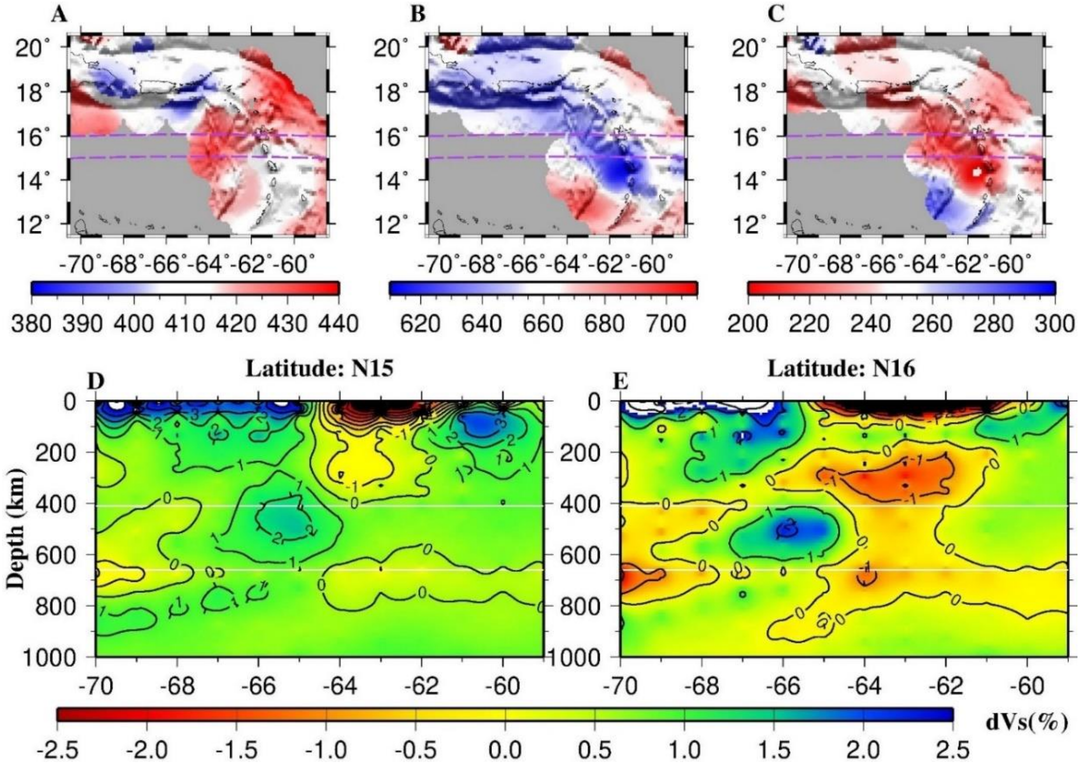

Figure 2. Spatial distribution of resulting apparent depths. (A) for the apparent d410. (B) Same as (A) but for the d660. (C) MTZ thickness measurements. (D) Cross section along the latitude N15° using US32 regional model (Zhu et al, 2020). Same as (D) but for latitude N16°.

3. LATERAL VARIATION IN MTZ STRUCTURE

For each of the stacked traces, the depths of two discontinuities in the depth ranges of 390-450 km and 630-690 km were automatically determined and marked on the trace. After manually checking to reject bins with weak arrivals or ambiguous peaks, a total of 64 bins with clearly observed d410 or d660 peaks were obtained, among which 58 have reliable d410, 61 has reliable d660, and 55 have both d410 and d660 determinations (Figure 1B, Table S1). All the 64 depth series plotted along the 9 latitudes (12°N-20°N with an increment of 1°) are shown in Figure S2.

Both of the resulting apparent d410 and d660 depths (Figure 2A and 2B) in the study area show systematic spatial variations ranging from 399 to 436 km and from 618 to 689 km, respectively. For the entire study area, the average apparent depths are 413.6±8.5 km and 654.8±12.7 km for the d410 and d660, respectively, and the mean MTZ thickness is 241.3±13.5 km (Figure 3C). The resulting apparent depth of the d410 is slightly deeper than the theorical values of 410 km in the IASP91 Earth model, while the apparent d600 is shallower than the theorical value, leading to a thinner than normal MTZ thickness beneath the study area.

In the central Lesser Antilles Subduction Zone, the apparently depressed d410 and uplifted d660 are both detected, causing the thinnest MTZ thickness (207 km) beneath this region, where a slab gap has been identified by previous tomographic images (van Benthem et al, 2013; Harris et al, 2018). Compared to the large cross-correlation coefficient (XCC) between the resulting apparent depth of d410 and d660, which is 0.84, for the contiguous United States (Gao and Liu, 2014), the XCC in our study is 0.28. Such low XCC may suggest the existence of significant lateral velocity variations in the MTZ. Based on the observations of regional tomographic images (Zhu et al., 2020), the existence of low S-wave velocity zone has been detected beneath the central Lesser Antilles Subduction Zone (Figure 2D and Figure 2E). The tomographic model indicates that the low velocity anomalies may originate from the lower mantle, affecting the apparent depths of the d660.

To eliminate the effects of velocity anomalies, we apply the velocity correction procedure to convert the apparent depths into true depths using three global and regional tomographic models (details can be found in Supplementary document). The results of average corrected depths, especially the corrected MTZ thickness, based on three tomographic models are similar to the apparent depths (Figure S3). The similarities between the apparent and corrected depths suggest that the velocity corrections did not effectively remove the influence of velocity heterogeneities on the observed MTZ discontinuity depths. Thus, the discussion on the thermal structures of the upper mantel and MTZ in the study region will mostly be dependent on the apparent depths.

4. THERMAL UPWELLING ASSOCIATED WITH SLAB GAPS

As it is mentioned before, the major factor that affect the MTZ discontinuities in our study area is thermal effect. The thinner MTZ thickness beneath central Lesser Antilles Subduction Zone is possibly caused by the high temperature, which depresses the d410 and uplifts the d660. As far as we know, the advective upwelling of hot materials can induce a higher temperature relative to the surrounding mantle in the MTZ. Such situation has been found in Alaska (Dahm et al., 2017), Indochina Peninsula (Yu et al., 2017), and Sumatra (Kong et al., 2020), where the thermal upwelling was detected through a slab window. The previous tomographic images in our study area have identified several slab gaps (van Benthem et al., 2013; Harris et al., 2018), which have the same effect as a slab window on thermal upwelling.

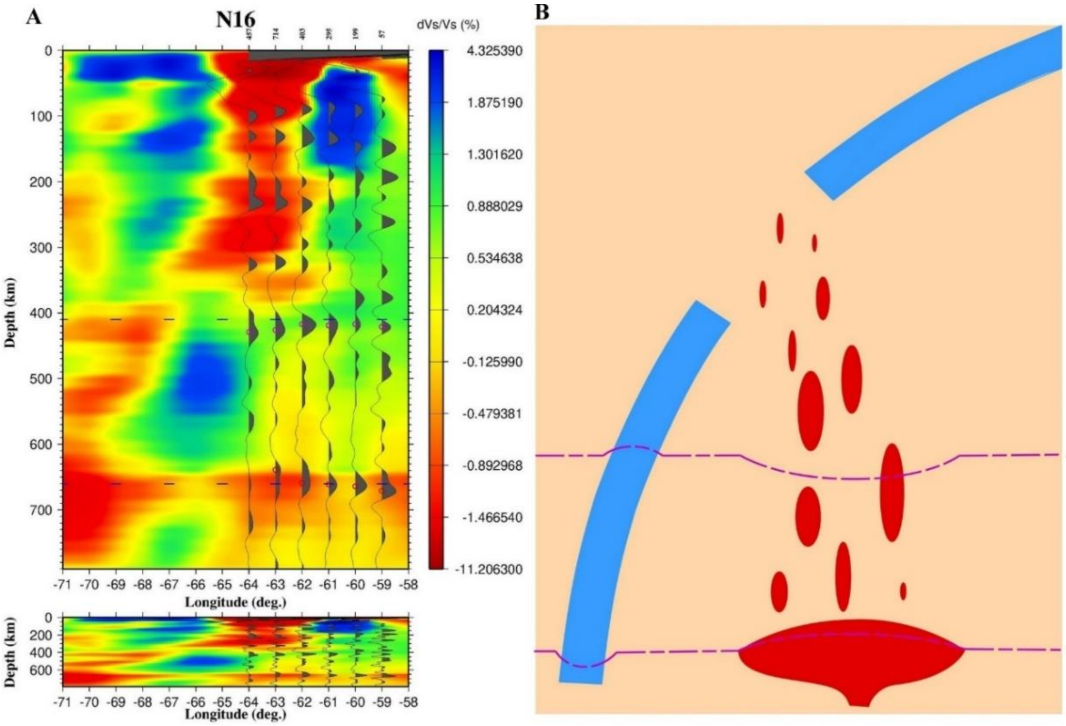

Figure 3. Cross sections of receiver function traces along the latitude N16°. (A) S-wave tomographic model using US32 (Zhu et al., 2020). (B) Schematic sketch of the Lesser Antilles Subduction Zone beneath our study area.

According to the previous studies, the different dip angles of the Wadati-Benioff zone under the Lesser Antilles Subduction Zone have been interpreted as two separate slab segments and proposed for the location of the plate boundary between the NA and SA (Wadge & Shepherd, 1984). Combined with the regional tomographic images (van Benthem et al., 2013; Harris et al., 2018), the slab gap between the northern Lesser Antilles and the southern Lesser Antilles is around 13°N – 15°N. The observed results along 15°N indicate that the average d410 discontinuities have been slightly depressed by

8 km and the average d660 discontinuities have been apparently uplifted by 17 km. One of the possible explanations for this thinner-than-normal MTZ is that thermal anomalies beneath the central Lesser Antilles Subduction Zone traverse the whole MTZ from the lower mantle. Assuming Clapeyron slopes of +2.9 Mpa/K and -1.3 Mpa/K for the d410 and d660 (Bina and Helffrich, 1994; Fei et al., 2004), respectively, the observed 25 km thinning of the MTZ corresponds to a ~ 210 K temperature increase in the MTZ. According to the regional tomographic model (Zhu et al, 2020), a low wavespeed zone has been identified at least 800 km beneath this region (Figure 2D and Figure 2E), suggesting the existence of a deep thermal upwelling beneath the central Lesser Antilles Subduction Zone (Figure 3) and the magmatism of active volcanoes around this region.

5. SLAB SEGMENTS IN THE MTZ

Numerous previous studies in the modern and ancient subduction zones (Dahm et al., 2017; Yu et al., 2018, Kong et al., 2020) have revealed the importance of the depth extent of cold slab segments in the MTZ discontinuity undulations. In the vicinity of this study area, several seismic tomographic images have suggested the existence of cold slab segments beneath the CA Plate (Bezada et al., 2010; van Benthem et al., 2013; Harris et al., 2018) with variable depth extents. The effect on the MTZ thickness undulation caused by the subducted slab depending on their depth extents (Dahm et al., 2017). If a slab penetrates the upper mantle and the entire MTZ, the resulting apparent and corrected depths of the d410 are shallower than normal because the d410 will be uplifted when the temperature in the upper MTZ decreases. The d660, however, is thicker than normal because the negative temperature anomaly will result in the depression of d660 due to the negative Clapeyron slope. A similar situation has been found in the southern Lesser Antilles Subduction Zone, which has a broader MTZ thickness (~ 15 km) caused by a close to normal d410 and an apparently depressed d660. According to the Clapeyron slopes for the d410 and d660 (Bina and Helffrich, 1994; Fei et al., 2004), the thicker value of MTZ thickness corresponds to a ~ 130 K temperature decrease in the MTZ. Based on the regional tomographic model, the oceanic portion of the SA Plate subducted beneath the southeastern part of the CA Plate, which is in the proximity of southern Lesser Antilles Subduction Zone and the slab dips steep and extends to a deep depth that larger than 600 km (Bezada et al., 2010). Combined with the localized wavespeed anomalies (Zhu et al, 2020), we believe that the subduction slab has penetrated through the d410 and traversed into the lower MTZ (Figure 3).

6. CONCLUSIONS

We use over 8000 P-to-S receiver functions from 1901 events recorded by 115 stations in eastern CA under the non-plane way assumption to image the 410 and 660 km discontinuities and map the spatial variation of the thickness of the MTZ. The receiver functions are grouped into circular bins with a radius of 1 degree and moveout corrected using the 1-D IASP91 Earth model prior to stacking. After doing the velocity correction based on the global earth model TX2019slab, UU-P07 and US32, the spatially variable MTZ thickness in the study area are mostly attributed to subducted cold slabs and thermal upwelling. In the southern Lesser Antilles Subduction Zone, a thicker than normal MTZ is attributed to the existence of cold slab segments, which is the oceanic SA lithosphere that subducted beneath the CA Plate. The thinner than normal MTZ observed in the central Lesser Antilles Subduction Zone is related to the mantle upwelling through the slab gap beneath this area. Also, the MTZ thinning in this region is mostly caused by an uplifted 660 km discontinuity, which suggests that the thermal upwelling may originate from the lower mantle.

APPENDIX

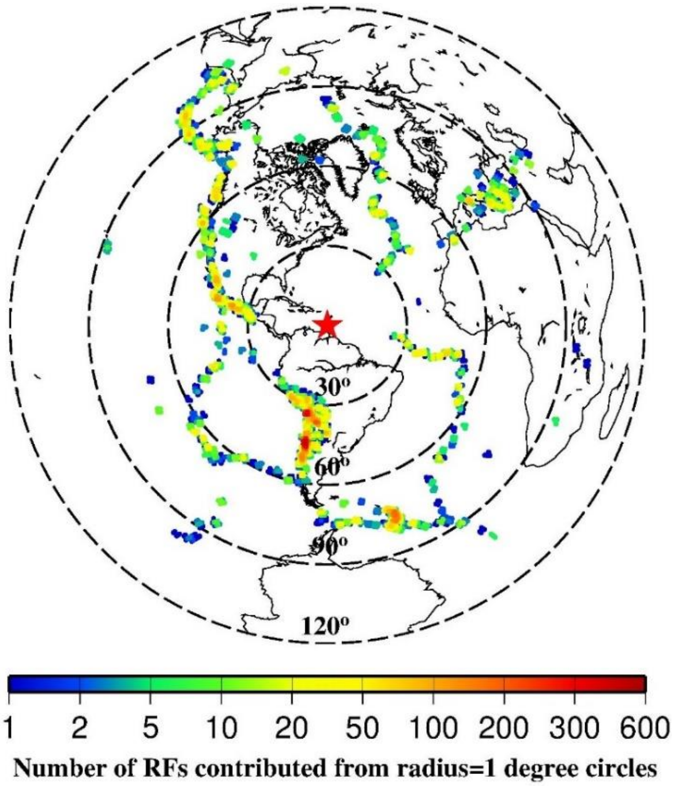

Figure S1. Spatial distribution of earthquake source areas. Each dot represents a radius = 1° circular area. The distance between neighboring circles is 1°. The color of the dot represents the number of used RFs that originated from earthquakes in the circle. The radius of the concentric dashed circles centered at the central part of the study area (red star) increased at a step of 30°.

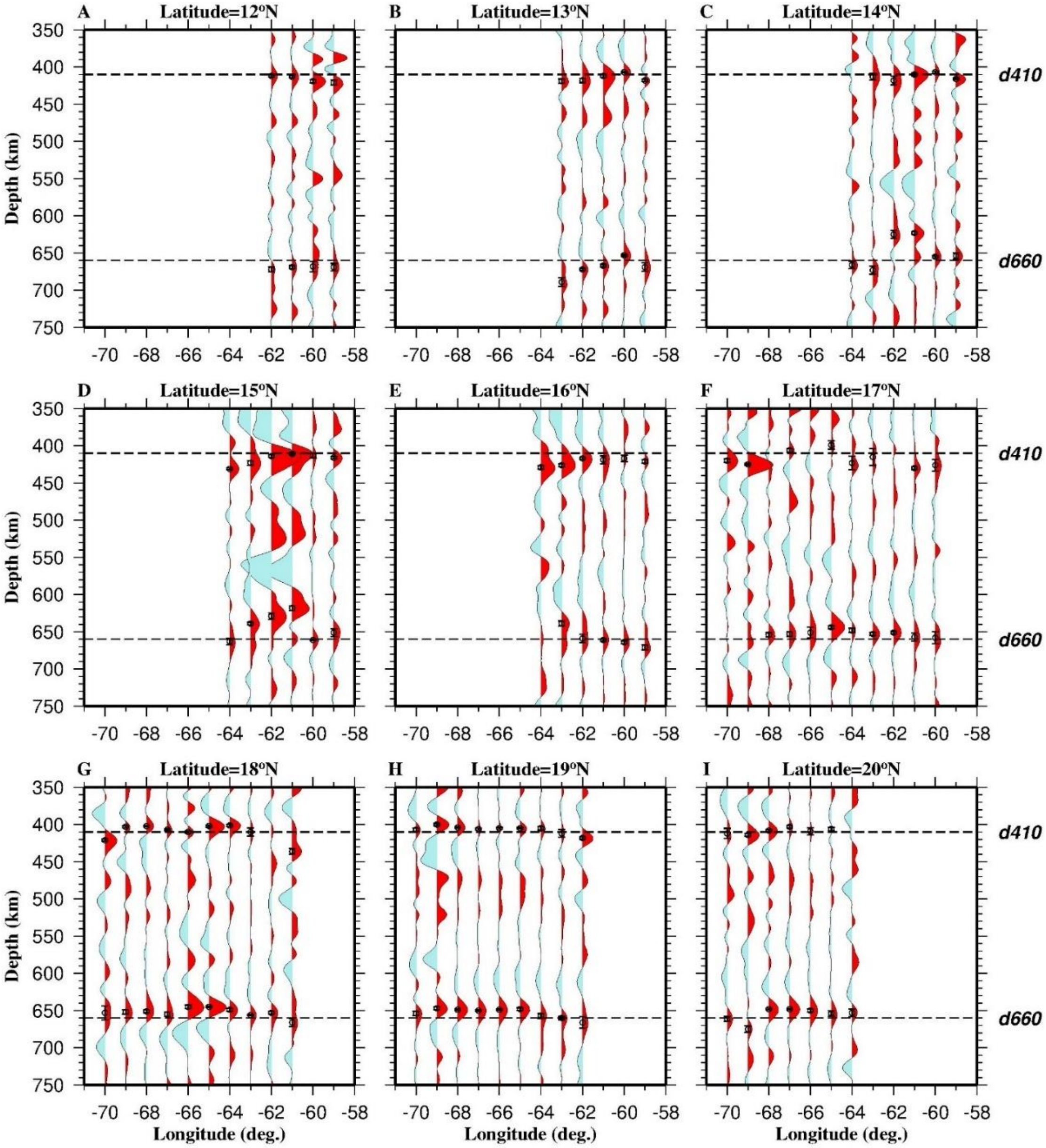

Figure S2. Results of stacking moveout-corrected RFs within each bin plotted along 12 latitude profiles. The black traces show the depth series averaged over all the 50 bootstrap iterations. The circles and error bars respectively represent the resulting apparent depths and standard deviations of the depths of the MTZS discontinuities.

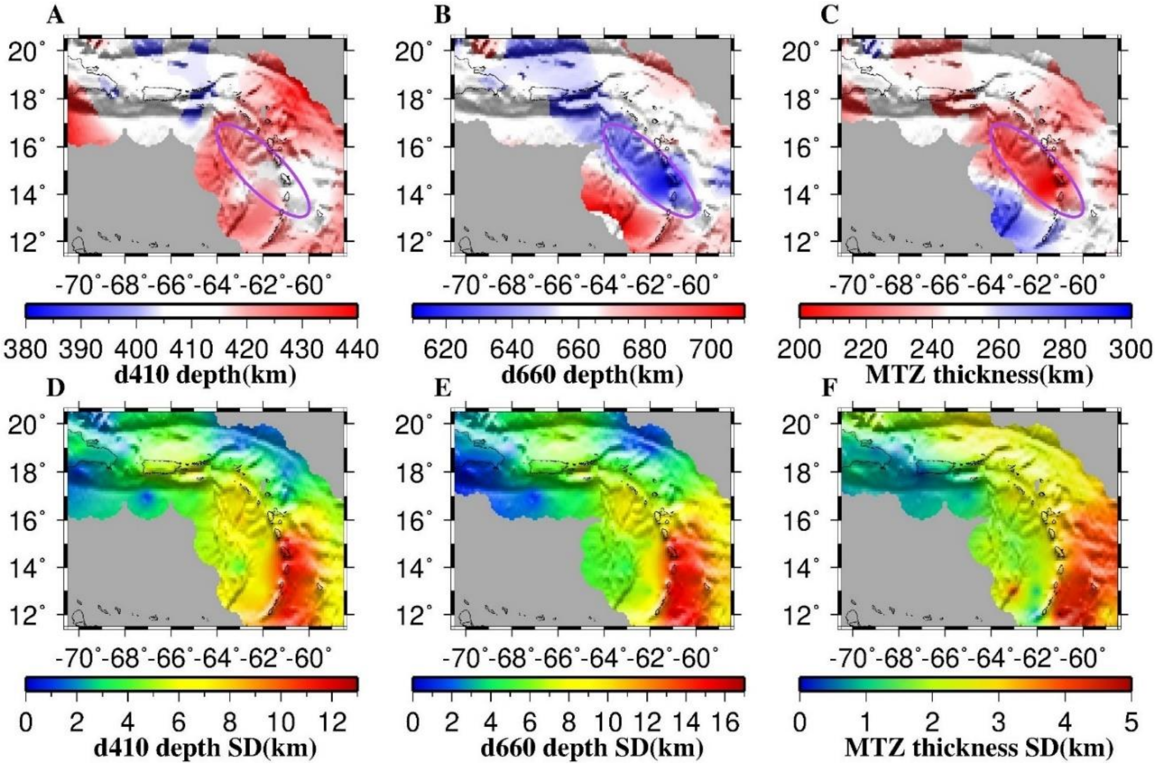

Figure S3. (A) Spatial distribution of resulting *d*410 corrected depths based on the average values of three different velocity model TX2019slab, UU_P07, US32. The purple circles mark the significant variation results. (B) Same as (A) but for the *d*660. (C) MTZ thickness measurements. (D) Standard deviation (SD) of the *d*410 depth. (E) SD of the *d*660 depth. (F) SD of the MTZ thickness measurements.

Table S1. Results of receiver function stacking for each bin.

clon	clat	d410	d410_sd	d660	d660_sd	MTZ	cd410	cd660	cMTZ
12	-59	421	0.05	669	0.03	247	421	668	247
13	-59	418	0.03	669	0.03	250	418	668	250
14	-59	416	0.03	654	0.02	237	416	652	237
15	-59	416	0.03	651	0.02	235	414	648	234
16	-59	421	0.03	671	0.04	250	420	669	249
12	-60	419	0.04	668	0.01	248	420	668	248
13	-60	407	0.04	653	0.03	246	408	653	245
14	-60	407	0.02	655	0.03	248	408	655	247
15	-60	413	0.02	661	0.03	247	412	659	247
16	-60	417	0.01	664	0.03	247	418	664	246
17	-60	426	0.02	658	0.02	232	426	658	232
12	-61	413	0.02	669	0.01	255	419	674	255
13	-61	412	0.02	667	0.01	255	417	672	255

Table S1. Results of receiver function stacking for each bin. (cont.)

14	-61	410	0.02	623	0.01	212	414	627	213
15	-61	411	0.03	618	0.03	207	413	619	207
16	-61	419	0.03	661	0.02	241	422	664	241
17	-61	430	0.03	657	0.03	226	430	657	227
18	-61	436	0.03	666	0.01	230	437	666	229
12	-62	412	0.02	672	0.01	260	421	684	263
13	-62	418	0.02	672	0.02	254	424	681	257
14	-62	418	0.02	625	0.01	207	420	629	209
15	-62	414	0.03	629	0.02	214	414	630	216
16	-62	417	0.04	659	0.02	241	418	660	242
17	-62	0	0.00	651	0.03	0	0	652	0
18	-62	0	0.00	653	0.03	0	0	654	0
19	-62	418	0.04	666	0.02	247	419	666	247
13	-63	419	0.02	689	0.01	270	425	702	276
14	-63	413	0.02	673	0.01	260	414	678	264
15	-63	423	0.02	639	0.02	216	420	638	218
16	-63	426	0.03	639	0.01	213	421	635	214
17	-63	415	0.01	653	0.02	238	416	652	237
18	-63	410	0.02	656	0.03	246	417	661	245
19	-63	412	0.01	660	0.03	248	415	662	246
14	-64	0	0.00	666	0.02	0	0	668	0
15	-64	431	0.03	663	0.02	232	429	664	235
16	-64	429	0.03	0	0.00	0	427	0	0
17	-64	423	0.02	648	0.01	224	424	648	225
18	-64	401	0.02	649	0.02	248	405	652	247
19	-64	405	0.01	657	0.02	251	407	658	252
20	-64	0	0.00	653	0.01	0	0	654	0
17	-65	399	0.01	644	0.02	244	401	647	246
18	-65	402	0.02	645	0.02	242	404	647	243
19	-65	405	0.01	648	0.02	242	404	647	243
20	-65	406	0.00	654	0.02	248	404	652	247
17	-66	0	0.00	651	0.01	0	0	651	0
18	-66	410	0.01	645	0.03	235	414	650	236
19	-66	405	0.01	649	0.03	244	405	649	244
20	-66	409	0.00	650	0.03	241	407	647	240
17	-67	406	0.01	653	0.01	246	411	660	249
18	-67	407	0.02	655	0.02	247	412	661	249
19	-67	406	0.01	650	0.03	243	409	652	244
20	-67	403	0.01	648	0.04	244	402	646	243

Table S1. Results of receiver function stacking for each bin. (cont.)

17	-68	0	0.00	654	0.02	0	0	652	0
18	-68	402	0.02	651	0.02	248	406	657	251
19	-68	404	0.02	649	0.03	245	410	655	245
20	-68	408	0.03	648	0.03	240	408	646	238
17	-69	425	0.04	0	0.00	0	425	0	0
18	-69	403	0.01	652	0.02	248	407	658	251
19	-69	400	0.02	647	0.02	247	404	651	248
20	-69	414	0.04	675	0.02	261	415	674	259
17	-70	420	0.05	0	0.00	0	419	0	0
18	-70	421	0.05	653	0.03	231	425	659	234
19	-70	407	0.02	654	0.03	247	411	658	248
20	-70	412	0.02	661	0.02	249	411	658	248

REFERENCES

Amaru, M. L. (2007). Global travel time tomography with 3-D reference models (Vol. 274). Utrecht University.

Ammon, C. J. (1991). The isolation of receiver effects from teleseismic P waveforms. Bulletin-Seismological Society of America, 81(6), 2504-2510.

Bezada, M. J., Levander, A., & Schmandt, B. (2010). Subduction in the southern Caribbean: Images from finite-frequency P wave tomography. *Journal of Geophysical Research: Solid Earth*, *115*(B12). https://doi.org/10.1029/2010JB007682

Bina, C. R., & Helffrich, G. (1994). Phase transition Clapeyron slopes and transition zone seismic discontinuity topography. *Journal of Geophysical Research: Solid Earth*, *99*(B8), 15853-15860. https://doi.org/10.1029/94JB00462

Collier, J. D., & Helffrich, G. R. (1997). Topography of the “410” and “660” km seismic discontinuities in the Izu-Bonin subduction zone. *Geophysical research letters*, *24*(12), 1535-1538. https://doi.org/10.1029/97GL01383

Dahm, H. H., Gao, S. S., Kong, F., & Liu, K. H. (2017). Topography of the mantle transition zone discontinuities beneath Alaska and its geodynamic implications: Constraints from receiver function stacking. *Journal of Geophysical Research: Solid Earth*, *122*(12), 10-352. https://doi.org/10.1002/2017JB014604

Fei, Y., Van Orman, J., Li, J., Van Westrenen, W., Sanloup, C., Minarik, W., ... & Funakoshi, K. I. (2004). Experimentally determined postspinel transformation boundary in Mg2SiO4 using MgO as an internal pressure standard and its geophysical implications. *Journal of Geophysical Research: Solid Earth*, *109*(B2). https://doi.org/10.1029/2003JB002562

Gao, S. S., & Liu, K. H. (2014). Mantle transition zone discontinuities beneath the contiguous United States. Journal of Geophysical Research: Solid Earth, 119(8), 6452-6468. https://doi.org/10.1002/2014JB011253

Harris, C. W., Miller, M. S., & Porritt, R. W. (2018). Tomographic imaging of slab segmentation and deformation in the Greater Antilles. *Geochemistry, Geophysics, Geosystems*, *19*(8), 2292-2307. https://doi.org/10.1029/2018GC007603

Hayes, G. P., Moore, G. L., Portner, D. E., Hearne, M., Flamme, H., Furtney, M., & Smoczyk, G. M. (2018). Slab2, a comprehensive subduction zone geometry model. Science, 362(6410), 58-61. DOI: 10.1126/science.aat4723

Helffrich, G. (2000). Topography of the transition zone seismic discontinuities. *Reviews of Geophysics*, *38*(1), 141-158. https://doi.org/10.1029/1999RG000060

Ito, E., & Katsura, T. (1989). A temperature profile of the mantle transition zone. *Geophysical Research Letters*, *16*(5), 425-428. https://doi.org/10.1029/GL016i005p00425

Kennett, B. L. N., & Engdahl, E. R. (1991). Traveltimes for global earthquake location and phase identification. *Geophysical Journal International*, *105*(2), 429-465. https://doi.org/10.1111/j.1365-246X.1991.tb06724.x

Kong, F., Gao, S. S., Liu, K. H., Ding, W., & Li, J. (2020). Slab dehydration and mantle upwelling in the vicinity of the Sumatra subduction zone: Evidence from receiver function imaging of mantle transition zone discontinuities. *Journal of Geophysical Research: Solid Earth*, *125*(9), e2020JB019381. https://doi.org/10.1029/2020JB019381

Langston, C. A. (1979). Structure under Mount Rainier, Washington, inferred from teleseismic body waves. Journal of Geophysical Research: Solid Earth, 84(B9), 4749-4762. https://doi.org/10.1029/JB084iB09p04749

Laurencin, M., Graindorge, D., Klingelhoefer, F., Marcaillou, B., & Evain, M. (2018). Influence of increasing convergence obliquity and shallow slab geometry onto tectonic deformation and seismogenic behavior along the Northern Lesser Antilles zone. *Earth and Planetary Science Letters*, *492*, 59-72. https://doi.org/10.1016/j.epsl.2018.03.048

Li, A., Fischer, K. M., Wysession, M. E., & Clarke, T. J. (1998). Mantle discontinuities and temperature under the North American continental keel. *Nature, 395*(6698), 160. https://doi.org/10.1038/25972

Litasov, K. D., Ohtani, E., Sano, A., Suzuki, A., & Funakoshi, K. (2005). Wet subduction versus cold subduction. Geophysical Research Letters, 32(13). https://doi.org/10.1029/2005GL022921

Lu, C., Grand, S. P., Lai, H., & Garnero, E. J. (2019). TX2019slab: A New P and S Tomography Model Incorporating Subducting Slabs. *Journal of Geophysical Research: Solid Earth*. https://doi.org/10.1029/2019JB017448

Meighan, H. E., Pulliam, J., ten Brink, U., & López-Venegas, A. M. (2013). Seismic evidence for a slab tear at the Puerto Rico Trench. *Journal of Geophysical Research: Solid Earth*, *118*(6), 2915-2923. https://doi.org/10.1002/jgrb.50227

Meschede, M., & Frisch, W. (1998). A plate-tectonic model for the Mesozoic and Early Cenozoic history of the Caribbean plate. *Tectonophysics*, *296*(3-4), 269-291. https://doi.org/10.1016/S0040-1951(98)00157-7

Pindell, J. L., & Barrett, S. F. (1990). Caribbean plate tectonic history. *The Caribbean Region, volume H of The Geology of North America*, 405-432.

Ringwood, A. E. (1975). Composition and Petrology of the Earth's Mantle. *MacGraw-Hill*, *618*.

Schlaphorst, D., Kendall, J. M., Baptie, B., Latchman, J. L., & Tait, S. (2017). Gaps, tears and seismic anisotropy around the subducting slabs of the Antilles. *Tectonophysics*, *698*, 65-78. https://doi.org/10.1016/j.tecto.2017.01.002

Shearer, P. M., & Flanagan, M. P. (1999). Seismic velocity and density jumps across the 410-and 660-kilometer discontinuities. *Science*, *285*(5433), 1545-1548. DOI: 10.1126/science.285.5433.1545

Sun, M., Fu, X., Liu, K. H., & Gao, S. S. (2018). Absence of thermal influence from the African Superswell and cratonic keels on the mantle transition zone beneath southern Africa: Evidence from receiver function imaging. *Earth and Planetary Science Letters*, *503*, 108-117. https://doi.org/10.1002/2017GL075485

Ten Brink, U. (2005). Vertical motions of the Puerto Rico Trench and Puerto Rico and their cause. *Journal of Geophysical Research: Solid Earth*, *110*(B6). https://doi.org/10.1029/2004JB003459

Tschauner, O., Ma, C., Beckett, J. R., Prescher, C., Prakapenka, V. B., & Rossman, G. R. (2014). Discovery of bridgmanite, the most abundant mineral in Earth, in a shocked meteorite. *Science*, *346*(6213), 1100-1102. DOI: 10.1126/science.1259369 van Benthem, S., Govers, R., Spakman, W., & Wortel, R. (2013). Tectonic evolution and mantle structure of the Caribbean. *Journal of Geophysical Research: Solid Earth*, *118*(6), 3019-3036. https://doi.org/10.1002/jgrb.50235

Wadge, G., & Shepherd, J. B. (1984). Segmentation of the Lesser Antilles subduction zone. *Earth and Planetary Science Letters*, *71*(2), 297-304. https://doi.org/10.1016/0012-821X(84)90094-3

Yu, Y., Gao, S. S., Liu, K. H., Yang, T., Xue, M., & Le, K. P. (2017). Mantle transition zone discontinuities beneath the Indochina Peninsula: Implications for slab subduction and mantle upwelling. *Geophysical Research Letters*, *44*(14), 7159-7167. https://doi.org/10.1002/2017GL073528

Zhu, H., Stern, R. J., & Yang, J. (2020). Seismic evidence for subduction-induced mantle flows underneath Middle America. Nature communications, 11(1), 1-12. https://doi.org/10.1038/s41467-020-15492-6

SECTION

2. CONCLUSIONS

In this study, we use 4915 XKS and 1202 pairs of local S wave splitting parameters from 24 stations investigate lithospheric deformation and asthenospheric flow beneath the boundary of the NA and CA plates and adjacent areas. The observations of seismic azimuthal anisotropy in the study region suggest the existence of two models to explain the distinct characteristics of XKS and local S measurements. The fast orientation in the NA plate is NNE-SSW, which is roughly orthogonal to the trench. This trench-perpendicular orientation indicates a corner flow induced by the steep subduction of the Cocos slab in the back arc. In contrast, the fast orientation on the CA plate is roughly parallel to the arc, which is WNW-ESE. The results of XKS and local S measurements suggest the coexistence of sub-slab mantle and mantle wedge beneath the CA plate. Due to the presence of slab window and the slab roll back, the Cocos sub-slab mantle travel through the slab window and entrain the mantle wedge along the MAT, causing the trench-parallel mantle flow beneath the CA plate and contributing to the formation of CAVA.

In eastern CA, we use over 8000 P-to-S receiver functions from 1901 events recorded by 115 stations under the non-plane way assumption to image the 410 and 660 km discontinuities and map the spatial variation of the thickness of the MTZ. The receiver functions are grouped into circular bins with a radius of 1 degree and moveout corrected using the 1-D IASP91 Earth model prior to stacking. After doing the velocity correction based on the global earth model TX2019slab, UU-P07, and US32, the spatially variable MTZ thickness in the study area can be mainly divided into six regions which are mostly attributed to subducted cold slabs and thermal upwelling. The thinner than normal MTZ observed in the northern Lesser Antilles Subduction Zone is caused by a high wave speed layer. In a part of the central Lesser Antilles Subduction Zone, a thicker than normal MTZ is attributed to the existence of cold slab segments, which is the oceanic SA lithosphere that subducted beneath the CA Plate, and the thermal upwelling influence in the surrounding area. For those regions around the central Lesser Antilles Subduction Zone, the thinner MTZ thickness is related to the mantle upwelling along the slab gaps in these areas. Also, the MTZ thinning in these regions are mostly caused by an uplifted 660 km discontinuity, which suggests that the thermal upwelling may originate from the lower mantle.

BIBLIOGRAPHY

Bernal-López, L. A., Garibaldi, B. R., Soto, G. L., Valenzuela, R. W., & Escudero, C. R. (2016). Seismic anisotropy and mantle flow driven by the Cocos slab under southern Mexico. *Pure and Applied Geophysics*, *173*(10-11), 3373-3393.

Castellanos, J., Pérez-Campos, X., Valenzuela, R., Husker, A., & Ferrari, L. (2017). Crust and upper-mantle seismic anisotropy variations from the coast to inland in central and Southern Mexico. *Geophysical Journal International*, *210*(1), 360-374.

León Soto, G., & Valenzuela, R. W. (2013). Corner flow in the Isthmus of Tehuantepec, Mexico inferred from anisotropy measurements using local intraslab earthquakes. *Geophysical Journal International*, *195*(2), 1230-1238.

van Benthem, S., Govers, R., Spakman, W., & Wortel, R. (2013a). Tectonic evolution and mantle structure of the Caribbean. *Journal of Geophysical Research: Solid Earth*, *118*(6), 3019-3036.

van Benthem, S. A., Valenzuela, R. W., & Ponce, G. J. (2013b). Measurements of upper mantle shear wave anisotropy from a permanent network in southern Mexico. *Geofísica internacional*, *52*(4), 385-402.

Huang, J., Vanacore, E., Niu, F., & Levander, A. (2010). Mantle transition zone beneath the Caribbean-South American plate boundary and its tectonic implications. *Earth and Planetary Science Letters*, *289*(1-2), 105-111.

LADD, J. W. (1976). Relative motion of South America with respect to North America and Caribbean tectonics. *Geological Society of America Bulletin*, *87*(7), 969-976.

Laurencin, M., Graindorge, D., Klingelhoefer, F., Marcaillou, B., & Evain, M. (2018). Influence of increasing convergence obliquity and shallow slab geometry onto tectonic deformation and seismogenic behavior along the Northern Lesser Antilles zone. *Earth and Planetary Science Letters*, *492*, 59-72.

Levander, A., Schmitz, M., Avé Lallemant, H. G., Zelt, C. A., Sawyer, D. S., Magnani, M. B., ... & Pindell, J. (2006). Evolution of the southern Caribbean plate boundary. *Eos, Transactions American Geophysical Union*, *87*(9), 97-100.

Meschede, M., & Frisch, W. (1998). A plate-tectonic model for the Mesozoic and Early Cenozoic history of the Caribbean plate. *Tectonophysics*, *296*(3-4), 269-291.

Pindell, J. L., & Barrett, S. F. (1990). Caribbean plate tectonic history. *The Caribbean Region, volume H of The Geology of North America*, 405-432.

VITA

Tu Xue was born in Shanghai, China. He received his bachelor’s degree in Geology & Geophysics from Missouri University of Science and Technology (Missouri S&T) in May 2017. He joined Dr. Gao and Dr. Liu’s research group in Geology & Geophysics program to pursue his Ph.D. degree at Missouri S&T in August, 2017.

During his graduate studies, he was actively involved in various academic activities. He was an active member in the American Geophysical Union (AGU), and Society of Exploration Geophysics (SEG). He presented his research works at AGU annual meeting in 2018 and 2019, and at GSA annual meeting in 2021. He was elected as the treasure of SEG at Missouri University of Science and Technology chapter during the year 2016 to 2018. His research focused on the structure and dynamic of the mantle and seismic anisotropy beneath Central America using receiver functions and shear wave splitting methods.

In December 2022 he received his Ph.D. degree in Geology & Geophysics from Missouri University of Science and Technology.